Journal of Physical Chemistry C, 2019, V. 123, P. 16091-16106; DOI: 10.1021/acs.jpcc.9b01219

Critical Conditions of Adhesion and Separation of Functionalized Nanoparticles on Polymer Grafted Substrates

Kolattukudy P. Santo[1], *Aleksey Vishnyakov*,[1,2] *Yefim Brun*[3] *and Alexander V. Neimark*[1*]

[1]Department of Chemical and Biochemical Engineering, Rutgers, The State University of New Jersey, Piscataway, N J, USA. [2]Skolkovo Institute of Science and Technology Moscow, Russia.

[3]DuPont Central research and Development, Wilmington, DE, USA

*Corresponding author: aneimark@rutgers.edu

Abstract:

Emerging technologies of production and processing of functionalized nanoparticles (NP) require advanced methods of NP characterization and separation. While various methods are available for NP separation by size, there are no efficient methods for NP separation by surface chemistry. Using extensive dissipative particle dynamics simulations, this work investigates the mechanisms of NP adhesion and flow in polymer brush (PB)-grafted pore channels searching for the conditions for size-independent separation of NPs that are similar to the critical conditions of liquid chromatography of polymers. We consider interactions of NPs functionalized by hydrophilic and hydrophobic ligands with PBs, in which conformation and adhesion properties are controlled by the solvent quality varied with the composition of thermodynamically good and poor solvent components. The NP-PB adhesion is characterized by the free energy landscape

calculated by the ghost tweezers simulation method that mimics the experimental technique of optical tweezers. The NP Henry constant and the respective partition coefficient are calculated depending on the NP size and ligand composition at varying solvent quality. Our findings demonstrate that with the decrease of solvent quality, the NP elution undergoes a transition from the size-exclusion mode with larger NPs having shorter retention time to the adsorption mode with the reverse order of elution. This transition, which occurs in a narrow range of solvent composition, signifies the so-called "critical" point of adsorption that strongly depends on the NP functionalization. The dynamics of NP axial dispersion in the isocratic and gradient elution modes is characterized employing a convective-diffusion model. We show that the NPs can be effectively separated by surface chemistry at the critical points of adsorption, using the gradient mode of interaction NP chromatography with controlled variation of the solvent composition.

I. Introduction

Nanoparticles (NPs) find numerous applications in biosensing,[1-2] imaging,[3] supercapacitors,[4] light emitting diodes (LEDs),[5-6] solar cells,[7-8] and nanoelectronic devices.[9] NPs functionalized with specific molecules are used in diagnostics and therapeutics,[10-11] as drug carriers, and nanoporous biomaterials.[12] Engineering and functional properties of NPs are sensitive to their size, shape, and surface chemistry, and advanced methods of NP characterization and separation are required for the quality control during NP production and processing. While various methods are available for NP separation by size and shape,[13-20] there are no efficient methods for NP separation by surface properties, such as the degree of hydrophobicity and surface heterogeneity, that are especially important in case of NPs modified by specific functional molecules or ligands.[21-23] It is highly desirable to develop techniques for NP chromatography based on the specifics of NP interactions with the stationary phase, reminiscent to the established techniques of interaction polymer chromatography.[24-26] Most beneficial would be a method capable of s*ize-independent separation of NPs* b*y surface chemistry* similar to the method of liquid chromatography at critical conditions (LCCC) for molecular weight independent separation of polymers by their composition and microstructure.[27-32]

The first advance in this direction was made in our recent work,[33] which explored the conditions of chromatographic separation of NPs on porous substrates grafted with polymer brushes in a binary mixture of thermodynamically "good" and "poor" solvents using dissipative particle dynamics (DPD) simulations. In this system, the PB played a role of a stationary phase to which NP may adhere and be retained. We showed that the NP adhesion depends on the PB conformation that is controlled by the solvent quality. For a particular system, it was

demonstrated that by varying the solvent composition it is possible to realize different separation modes with the transition from the size exclusion mode with larger particles having shorter retention time, which is characteristic to conventional separation techniques of size exclusion (SEC)[17] and hydrodynamic (HDC)[18] chromatography, to the adsorption mode with the reverse sequence of elution. In the present paper, we consider separation of NPs functionalized by different types of ligands and show that the crossover between the size exclusion and adsorption modes occurs for NPs of given surface chemistry in a narrow range of solvent compositions with approximately size-independent elution, similarly to the critical conditions of adsorption observed in polymer separation by LCCC. These findings lay out a foundation for the *interaction NP chromatography at critical conditions* (INPCC) and inform the design of chromatographic columns and solvent selection for efficient separation of NPs by surface chemistry.

The specifics of NP-PB interactions play the central role in the process of NP separation on polymer grafted substrates, as well as in various applications of NP-PB systems such as PBs doped by NPs used in sensors and biomedical devices,[34] fabrication of nanocomposites,[35-37] lubrication,[38] stabilization of colloids,[39-41] and manipulation of nanoobjects on surfaces.[42] Utilization of PB-grafted substrates in NP separation in the SEC has been investigated recently.[43] NP adhesion to PBs can be controlled by varying the solvent composition[44-45] that affects the PB conformation. Upon worsening of solvent quality and respective PB contraction, the free energy of NP-PB adhesion generally decreases and adhesion becomes stronger, as a result of competing effects of enthalpic attraction between polymer and NP ligands and entropic repulsion due to NP immersion into PB. The entropic effects dominate when PB is expanded in good solvent, while the enthalpic effects dominate when PB is collapsed in bad solvent. As shown in ref. 33, the NP elution in a PB grafted channel undergoes a transition from the completely repulsive size

exclusion mode in the good solvent to an adsorption mode upon addition of the poor solvent component. This observation suggested a possibility of existence of so-called critical point of adsorption (CPA),[24] at which the entropic and enthalpic effects are compensated and the NP elution is size-independent as in the LCCC. In this work, we confirm this hypothesis and show that the CPA of functionalized NP to PB in binary solvent can be defined as a particular solvent composition, which corresponds to the transition between the size exclusion and adsorption modes and depends on the NP surface chemistry. Note that in contrast to polymer adsorption, the introduced CPA of NP adhesion to PB is not related to any critical phenomenon, but it rather indicates a condition of the observed sharp transition from the entropy-dominated to enthalpy-dominated regimes leading to the reversal of the size-dependent sequence of elution.

In search for the CPA conditions of size independent elusion, we perform extensive DPD simulations to investigate the effects of the NP surface chemistry on NP adhesion and flow in PB-grafted pore channels in a binary solvent at different solvent composition. We consider NPs functionalized by two different kinds of ligands, which are modeled as short hydrophobic and hydrophilic chains grafted on the NP surface. By varying the ligand composition, we mimic different surface chemistries and control the NP-PB adhesion interaction. We analyze the specifics of solvent flow through PB-grafted channels and quantify the morphology and sorption capacity of the PB stationary phase depending on the solvent composition by introducing the hydrodynamic PB thickness as the stationary phase boundary. The NP-PB adhesion is quantified in terms of the free energy landscape, calculated using the Ghost Tweezers (GT) method,[45] which determines the Henry constant of NP adsorption, the partition coefficient, and ultimately the NP retention time, depending on the solvent and ligand compositions. The NP retention time distribution is analyzed using the convective-diffusion model. For NP of different surface

chemistry, we identified the CPA solvent composition that corresponds to a transition between the size exclusion to adsorption modes. The relationship is established between the solvent composition at CPA and the NP ligand composition that points toward a possibility of efficient NP separation by surface chemistry in the solvent gradient regime by varying the solvent composition as it is done in the gradient elution regime of interaction polymer chromatography.[29-30]

The following text is structured as follows. Section II discusses the simulation models and methods which include a brief description of the DPD method, system set up, coarse-graining scheme, parameterization of the model, the ghost tweezer method and solvent flow simulations. Section III discuses our theoretical models and results from the simulations: the calculation of free energy of NP adhesion to PB using the ghost tweezers technique from which the Henry constant and partition coefficient of NPs are derived, and the prediction of NP motion through PB-grafted channels and NP retention times based on the calculated polymer density profiles, thermodynamics calculation, and the solvent velocity profiles obtained in separate simulations. This section also discusses a macroscopic model for NP elution in a cylindrical channel in the *isocratic (no solvent gradient)* mode, in terms of "first passage time" distributions based on a convective-diffusion model, and the prediction of separation of our model NPs in solvent *gradient* elution mode of NP chromatography, utilizing the results of free energy profiles and flow calculation, along with discussion of some practical aspects of our findings. Section IV concludes our work.

II. Models and Methods

II. I. Dissipative Particle Dynamics. DPD[46-48] employs a coarse-grained (CG) scheme where atoms are lumped together into beads that interact with soft-core repulsive potentials allowing for possible overlap between the beads. In DPD simulations, the beads move according to Newton's equations of motion governed by the pairwise interaction potentials; the total force $\boldsymbol{F}_i$ on the i^{th} particle is presented as,

$$\mathbf{F}_i = \sum_{j \neq i} (\mathbf{F}_{ij}^{(\mathrm{C})} + \mathbf{F}_{ij}^{(\mathrm{B})} + \mathbf{F}_{ij}^{(\mathrm{D})} + \mathbf{F}_{ij}^{(\mathrm{R})}) \tag{1}$$

Here, $\mathbf{F}_{ij}^{(\mathrm{C})} = a_{ij}\left(1 - r_{ij}/R_{\mathrm{c}}\right)\hat{\boldsymbol{r}}_{ij}$ for $r_{ij} = \left|\mathbf{r}_i - \mathbf{r}_j\right| \leq R_{\mathrm{c}}$, is the conservative force between beads i and j, where a_{ij} is the repulsion parameter and R_c is the interaction range beyond which the conservative force vanishes; R_{c} represents the effective diameter of the beads. The drag forces $\boldsymbol{F}_{ij}^{(\mathrm{D})}$ and the random forces $\boldsymbol{F}_{ij}^{(\mathrm{R})}$,

$$\mathbf{F}_{ij}^{(\mathrm{D})} = -\gamma\, w^{(\mathrm{D})}(r_{ij})\left(\hat{\mathbf{r}}_{ij}.\mathbf{v}_{ij}\right)\hat{\mathbf{r}}_{ij}; \qquad \mathbf{F}_{ij}^{(\mathrm{R})} = \sigma w^{(\mathrm{R})}(r_{ij})\theta_{ij}\hat{\mathbf{r}}_{ij} \tag{2}$$

constitute the Langevin thermostat; γ is the friction coefficient, $\sigma^2 = 2\gamma kT$ and $\mathbf{v}_{ij} = \mathbf{v}_i - \mathbf{v}_j$ is the relative velocity between i^{th} and j^{th} beads. The weight functions $w^{(\mathrm{D})}$ and $w^{(\mathrm{R})}$ are related[48] as $w^{(\mathrm{D})} = (w^{(\mathrm{R})})^2$ with $w^{(\mathrm{R})}(r_{ij}) = \left(1 - r_{ij}/R_c\right)$ [46] for $r_{ij} \leq R_{\mathrm{c}}$ and zero for $r_{ij} > R_{\mathrm{c}}$. θ_{ij} is a random variable with Gaussian statistics. In addition, the bonded beads interact via harmonic bond forces $\mathbf{F}_{ij}^{(\mathrm{B})} = -k_{\mathrm{bond}}\left(r_{ij} - r_{\mathrm{e}}\right)\hat{\mathbf{r}}_{ij}$ where k_{bond} is the effective bond rigidity and r_{e} is the equilibrium bond length.

As an instructive example, we consider a model polymer - binary solvent system consisting of polyisoprene natural rubber (PINR), benzene as a good solvent and acetone as a poor solvent that was parameterized and studied in our previous works.[33, 44-45] We employ the most common implementation of DPD[46] with the all beads having the same effective diameter R_{c} = 0.71 nm. Because the persistence length of PINR in acetone-benzene solutions is very short,

about $2R_c$,[44] introduction of additional bond and angle potentials is not necessary. DPD simulations are performed in reduced units with R_c as the unit of length and k_BT as the unit of energy with friction coefficient $\gamma = 4.5$ at a time step of $0.02\ \tau_{DPD}$, where τ_{DPD} is the unit of DPD time. Since conversion of the DPD time unit τ_{DPD} into physical units is not unequivocal, we used the experimental benzene self-diffusion coefficient ($2.21 \times 10^{-5}\ cm^2/s$ [49]) as a reference property. Comparing the simulated value of the benzene diffusion coefficient in pure benzene ($0.22\ R_c^2/\tau_{DPD}$) with the experimental, we get $\tau_{DPD} \approx 50ps$. It should be noted that the conversion between the reduced and the real time units does not affect the elution time calculations (Section III.I)

Simulations were performed with LAMMPS[50] software package. The systems contained 0.3 to 0.4 million particles, and these massive parallel simulations consumed about 200000 CPU hours altogether. Configuration snapshots were created using the Visual Molecular Dynamics (VMD) program.[51]

II. II. System set up. PB is composed by linear chains of length n_{seg} composed by ***P*** beads representing PINR monomer, which are connected by harmonic bonds. The good and poor solvent components are modeled as single beads, ***G*** and ***B*** (see Fig. 1a). ***G*** bead corresponds to one hydrophobic benzene molecule, and ***B*** bead corresponds to one polar acetone molecule. NPs are built as spherical aggregates of radius R_{NP}, consisting of beads close-packed on an HCP lattice and connected by strong harmonic bonds holding the structure intact with the number density close to $3R_c^{-3}$. NPs have a core-shell structure with the shell consisting of two layers of surface ***N***-beads that interact with solvent, ligand, and polymer beads and the core consisting of ***C***-beads that strongly repel all other beads except for surface beads (Fig. 1b). The core-shell NP structure prevents penetration of mobile beads inside the NP. We consider NPs of three different

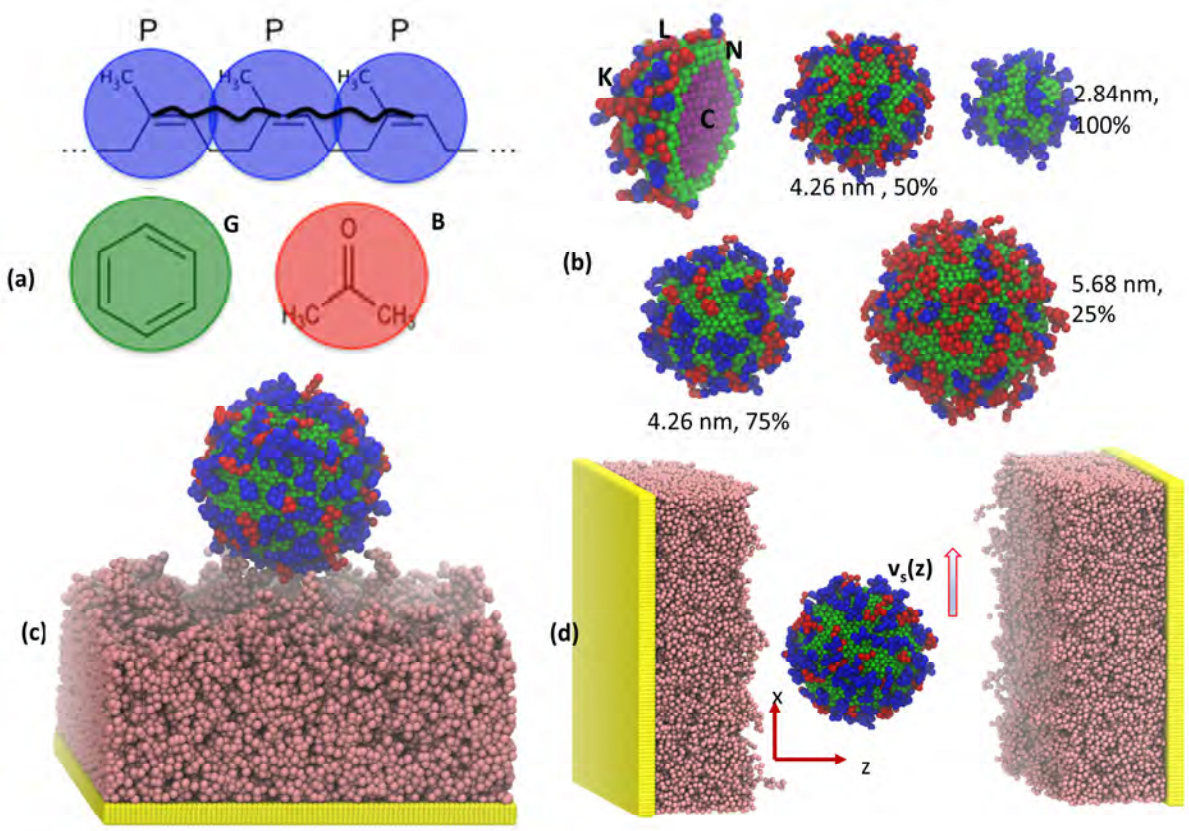

Figure 1. (a) The coarse-graining scheme of polymer (PINR) and good (benzene) and poor (acetone) solvent components. (b) NPs of different size consisting of core beads **C** and surface beads **N** functionalized by hydrophobic ***L*** (red) and hydrophilic ***K*** (blue) short chain ligands; degree of hydrophilicity is characterized by the fraction x_K of **K** ligands. (c) Simulation set-up for calculating the free energy landscapes using the GT method. PB chains (pink) are grafted on the substrate (yellow) surface and NP is restrained by the GT (not shown). (d) Simulation set-up for modeling NP flow in a slit-like channel with PB-grafted walls. The steady flow of solvent beads (not shown) has a Poiseuille-like velocity profile $v_s(z)$ in the X-direction.

sizes with radii, $R_{\mathrm{NP}} = 4\,R_{\mathrm{c}}\,, 6\,R_{\mathrm{c}}$ and $8\,R_{\mathrm{c}}$, which correspond to the NP diameters of 5.68, 8.52, and 11.36 nm, consisting of total number of beads $n_{\mathrm{NP}} = 740$, 2496, and 5917, respectively.

The surface chemistry is modeled with "ligands", short 6-bead long chains attached uniformly to the NP surface with strong harmonic bonds. We consider two types of ligands having distinct interaction properties, denoted as ***L*** (hydrophobic, favorably interacting with the polymer) and ***K*** (hydrophilic, unfavorably interacting with the polymer), and control the NP surface chemistry by varying the ligand composition; the *degree of NP hydrophilicity* is

characterized by the fraction $x_{\mathbf{K}} = n_{\boldsymbol{K}}/(n_{\boldsymbol{L}} + n_{\boldsymbol{K}})$ of $\boldsymbol{K}$ ligands, where $n_{\boldsymbol{L}}$ and $n_{\boldsymbol{K}}$ are respectively the number of $\boldsymbol{L}$ and $\boldsymbol{K}$ ligands on the NP surface.

To construct PB, polymer chains are grafted on a solid substrate that consists of densely packed immobile $\boldsymbol{S}$-beads with density of 19 R_{c}^{-3}, forming a flat surface of area $40 \times 40\ R_{\mathrm{c}}^{2}$ in the X-Y plane as shown in Fig.1c. In most of the simulations in this work, PB is comprised of chains containing $n_{\mathrm{seg}} = 90$ P-beads that are grafted to the substrate uniformly with the surface density of $\Gamma = 0.3025\ R_{\mathrm{c}}^{-2} (0.6\ \mathrm{nm}^{-2})$, which corresponds to 484 chains in total (this system is denoted below as PB1). A few selected simulations are also performed with the reduced PB density $\Gamma = 0.1806\ R_{\mathrm{c}}^{-2} = 0.36\ \mathrm{nm}^{-2}$ and longer chain length $n_{\mathrm{seg}} = 160$ (PB2) and with the same PB density and $n_{\mathrm{seg}} = 200$ (PB3). The system is kept at constant density equal to the bulk solvent density $\rho_{\mathrm{b}} = \rho_0 = 3\ R_{\mathrm{c}}^{-3}$. The solvent quality is controlled by the fraction of the good solvent $\boldsymbol{G}$-beads in the solvent, $x_{\boldsymbol{G}} = n_{\boldsymbol{G}}/(n_{\boldsymbol{B}} + n_{\boldsymbol{G}})$ which varies in the simulations from 1 to 99%. On average, simulation systems for free energy calculations contain about 0.3 million particles while the systems of solvent flow contain about 0.4 million particles. Altogether, we performed 1,700+ simulations of ≥1 million simulation steps.

II. III. Interaction parameters. The interaction parameters for solvent and polymer are taken from our previous works[33, 44-45] and are presented in Table I. The intracomponent repulsion parameter $a_{ii} = 42\ k_B T/R_c$ for all beads, that effectively reproduces the solvent compressibility.[44] NP core $\boldsymbol{C}$-beads strongly repel all other beads: $a_{\mathbf{C}i} = 60\ k_{\mathrm{B}}T/R_{\mathrm{c}}$. NP surface $\boldsymbol{N}$-beads effectively attract polymer $\boldsymbol{P}$-beads, as $\Delta a_{\boldsymbol{NP}} = a_{\boldsymbol{NP}} - a_{\boldsymbol{NN}} = -3.5\ k_{\mathrm{B}}T/R_{\mathrm{c}}$ ($a_{ij} < a_{ii}$ leads to an effective attraction between i and j bead types). The polymer $\boldsymbol{P}$-beads interact with good solvent $\boldsymbol{G}$-beads with very weak repulsion $\Delta a_{\boldsymbol{PG}} = 1.5\ k_{\mathrm{B}}T/R_{\mathrm{c}}$ and are repelling poor

Table 1. List of repulsion and bond parameters of the DPD beads in the simulations.

Repulsion parameter a_{ij}

i/j	C	N	L	K	A	P	G	B	S
C	42.0	60.0	60.0	60.0	0.0	60.0	60.0	60.0	60.0
N		42.0	42.0	42.0	0.0	38.5	43.5	43.5	42.0
L			42.0	42.0	0.0	42.0	43.5	49.0	42.0
K				42.0	0.0	46.0	47.5	43.5	42.0
A					0.0	0.0	0.0	0.0	0.0
P						42.0	43.5	49.0	42.0
G							42.0	43.5	42.0
B								42.0	42.0
S									42.0

Bond parameters		
Bond	k_{bond} ($k_{\mathrm{B}}T/R_{\mathrm{c}}^2$)	r_{e} (R_{c})
$C-C, N-N, N-C, L-L, L-N, K-K, K-L, P-P$	120	0.8
NP-GT	0.01	0.0

solvent B-beads with $\Delta a_{PB} = 7.0\ k_{\mathrm{B}}T$. Hydrophobic L-bead is similar to polymer P-bead with the same interaction parameters with the solvent components. Hydrophilic K-beads repel P-beads with $\Delta a_{KP} = 4.0\ k_{\mathrm{B}}T/R_{\mathrm{c}}$, and interact with solvent beads in the opposite manner strongly repulsive to good solvent G-beads, $\Delta a_{KG} = 5.5\ k_{\mathrm{B}}T$, and weakly repulsive to bad solvent B-beads, $\Delta a_{KB} = 1.5\ k_{\mathrm{B}}T$. Note that the mismatch parameter between the good and poor solvents $\Delta a_{GB} = 1.5\ k_BT$ is chosen to reflect the fact that the acetone and benzene are miscible and do not phase separate to form an interface. The total density of ligands on NPs is fixed to $0.198\ R_{\mathrm{c}}^{-2}$ ($0.39\ \mathrm{nm}^{-2}$). To control the surface properties, the fraction of ligand K, x_K is varied from 0 to 100%. All the interaction parameters are listed in Table 1.

II. IV. The Ghost Tweezer Method. In order to analyze the specifics of NP adhesion to PB and calculate the Henry constant and partition coefficient between mobile and stationary phases, we determine the free energy landscape of NP adhesion to PB by the ghost tweezers method,[45] which *in silico* mimics optical or magnetic tweezers experiments. In the GT method, NP is

tethered at given position using its immobile identical twin (called the 'ghost tweezers particle') which is pinned at this point and does not interact with any other beads. NP composed of n_{NP} beads is linked to GT by n_{NP} inter-bead harmonic bonds connecting each NP bead with the corresponding bead in GT. GT beads are denoted as $\boldsymbol{A}$-beads, which do not interact with any system component, $a_{\boldsymbol{AA}} = a_{\boldsymbol{Ai}} = 0$. The NP-GT inter-bead harmonic potential is weak, of strength $k_{\mathrm{GT}} = 0.01\ k_{\mathrm{B}}T/R_{\mathrm{c}}^2$ (see Table 1) and equilibrium position $r_{\mathrm{e}} = 0$, yet multiple inter-bead bonds control NP fluctuations and prevent its rotation. Far from PB, in the absence of external forces, NP fluctuates around GT.

In the course of simulation, NP is towed by GT in Z-direction towards the substrate in small increments allowing for the system equilibration at each incremental step. When GT is placed close enough to the substrate, NP interacts with PB, the force acting on NP from PB is counterbalanced by the force exerted on NP by the GT through its n_{NP} inter-bead harmonic bonds. Since the PB is symmetric in X and Y directions, the average force in these directions is zero, and the force exerted by GT in normal direction, $F_{\mathrm{GT}} = -k_{\mathrm{GT}} \sum_{i=1}^{n_{\mathrm{NP}}} (z_{\mathrm{NP}}^i - z_{\mathrm{GT}}^i)$, where z^i is the distance of the i^{th} bead from the substrate surface. Thus, one can measure the strength of NP-PB interaction by averaging the GT force, $\bar{F}_{\mathrm{GT}}(\bar{z}) = -K_{\mathrm{GT}}(\bar{z} - Z_{\mathrm{GT}}) = -K_{\mathrm{GT}}\Delta z$, where $\bar{z}$ and Z_{GT} are, respectively, the average center of mass Z-coordinates of NP and its GT twin, $\Delta z = (\bar{z} - Z_{\mathrm{GT}})$ and $K_{\mathrm{GT}} = n_{\mathrm{NP}} k_{\mathrm{GT}}$, is the cumulative spring constant. Initially, when the GT is placed in the bulk solvent far enough from PB, NP fluctuates about the GT position with $\Delta z = 0$ and average NP-GT force $\bar{F}_{\mathrm{GT}} = 0$. Then, NP is pulled towards the substrate by displacing GT in successive incremental steps of $\Delta \mathrm{Z}_{\mathrm{GT}} = 0.5\ R_{\mathrm{c}}$. The system is equilibrated at each step to measure the average NP position $\bar{z}$ and, respectively, the average force exerted by PB on NP,

$\bar{F}_{\mathrm{GT}}(\bar{z})$. The free energy $A(z)$ of NP-PB interaction is the mechanical work that is required to bring the NP to the point z above the substrate from the bulk, obtained by integrating $\bar{F}_{\mathrm{GT}}(\bar{z})$

$$A(z) = \int_{z_0}^{z} \bar{F}_{\mathrm{GT}}(\bar{z}) d\,\bar{z} \tag{3}$$

The NP location z_0 far from the substrate serves as a reference point where $A = 0$.

The system set up for free energy calculation is shown in Fig. 1c, where the NP that is functionalized with short ligands is placed above PB grafted on a solid substrate. The normal dimension of the simulation box is chosen in the range of 50 – 56 R_{c} to prevent overlapping of PBs on the opposite channel walls and provide NPs with enough space in the channel center to equilibrate in the bulk solvent, without hinders arising from the periodic boundary conditions. Mainly, four sets of systems corresponding to NPs having hydrophilic $\boldsymbol{K}$ ligand fraction or the degree of hydrophilicity, $x_{\boldsymbol{K}}$ =0.25, 0.5, 0.75 and 1.00 are simulated. The case of NPs with entirely hydrophobic (attractive to polymer) ligands $\boldsymbol{L}$, corresponding to $x_{\boldsymbol{K}} = 0$, was studied in our previous work.[33] In each system, the free energy landscape is calculated for NPs of 3 different radii R_{NP} of $4R_{\mathrm{c}}$ (2.84 nm), 6 R_{c}(4.26 nm) and 8 R_{c} (5.68 nm), in solvents of different quality characterized by the fraction $x_{\boldsymbol{G}}$ of the good solvent component. Most simulations are performed with PB grafting density 0.6 nm^{-2} (system PB1). A few additional simulations with PBs of grafting density 0.36 nm^{-2} and polymer lengths n_{seg} =160 (PB2) and 200 (PB3) are also performed to demonstrate the specifics of NP-PB interactions at poor solvent conditions (low $x_{\boldsymbol{G}}$). The free energy landscape $A(z)$ is calculated at a spatial resolution of 0.5 R_{c}. Altogether, a total of approximately 1100 simulations of 1 million timesteps with 0.28 to 0.31 million particles are performed.

II. V. Solvent flow simulations. Simulations of the solvent flow are performed in the slit channel between two identical PB-grafted walls with Z being the normal and X (direction of flow) and Y being lateral directions (Fig.1d). The size of the simulation cell is $40 \times 40 \times 70\ R_c^3$, which corresponds to the channel width $2w \approx 66.75\ R_c = 47.4$ nm (subtracting the wall thickness on both sides). A steady flow is created by applying a constant force g (of magnitude g = 0.002 $k_B T/R_c$) to the solvent particles, at different good solvent fraction ranging from 1 to 99%. The solvent velocity profile across the channel $v_s(z)$ is obtained by averaging over 100,000 steps after the system equilibration for 500,000 steps.

III. Results and Discussion

III. I. Solvent flow Through Polymer Brush-grafted Channels. We perform simulations of flow of binary solvent through PB-grafted slit-like channels between two identical PB-grafted walls at different solvent compositions. The simulations help to understand how the flow is affected by the conformation of PB which is determined by the solvent quality. Fig. 2a shows the respective density profiles of PB (system PB1) and solvent at different good solvent fractions within the entire range of solvent quality from x_G= 0.01 to 0.99. As the solvent quality worsens, the PB layer contracts and gradually becomes denser and thinner, expelling the solvent from its interior; the PB density profile, $\rho_{PB}(z)$, becomes sharper. The solvent density outside PB equals the bulk density ρ_b, while inside it is $\rho_s(z) = \rho_b - \rho_{PB}(z)$. Note that if an interfacial region is defined between PB and the bulk solvent, then the width of this interfacial region reduces as x_G decreases and becomes very narrow in the completely collapsed state at $x_G = 0.01$.

The simulated velocity profiles $v_s(z)$ at various solvent compositions are shown in Fig. 2b as dashed lines. The flow does not penetrate into PB with the solvent inside PB being

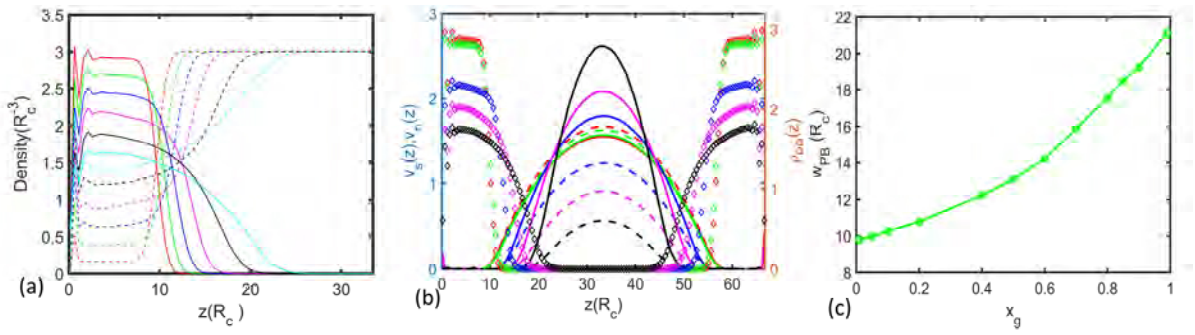

Figure 2. (a) The PB (solid lines) and binary solvent (dashed lines) density profiles along z at different solvent composition: x_G= 0.01 (red), 0.20 (green), 0.40 (blue), 0.60 (magenta), 0.80 (black) and 0.99 (cyan). PB contracts as the solvent quality worsens. (b) Normalized (solid lines) and simulated (dashed lines) solvent velocity profiles across the channel along with PB density profiles (diamonds) at different solvent composition: x_G=0.05 (red), 0.10 (green), 0.50 (blue), 0.70 (magenta) and 0.90 (black). Solvent flow does not penetrate PB and is similar to the Poiseuille flow confined to the mobile phase with no-slip conditions set at the outer boundary of PB determined by the PB hydrodynamic thickness w_{PB}. Simulations are at the same applied force g = 0.002 k_BT/R_c and the simulated velocity magnitude increases as the solvent quality worsens and the PB contracts. The normalized velocities represent the predicted solvent flows at the condition of the constant solvent flux. The magnitude of the normalized velocity decreases as the PB contracts and mobile phase volume increases. (c) The variation of the PB hydrodynamic thickness w_{PB} with the good solvent fraction x_G. The PB hydrodynamic thickness w_{PB} represents the extension of the stationary phase.

effectively stagnant. In all our simulations, the same force is applied to the solvent particles. As the result, as the solvent quality x_G decreases and the PB contracts, the resistance to the flow reduces and the velocity increases. As such, the computed total flux depends on the solvent composition. However, comparison of the effect of the solvent composition on the flow and NP retention has to be done at the condition of the constancy of the total flux. This is ensured by using the normalized velocities, which secure this condition. As shown in the previous work,[33] the simulated solvent velocity $v_s(z)$ is similar to the Poiseuille flow with no-slip conditions set at the outer boundary of PB. The solvent velocity may be approximated as a parabola, $v_s^{PA}(z) = v_m\left(1-\frac{(w-z)^2}{(w-w_{PB})^2}\right)$, where v_m is the maximum solvent velocity observed at the channel center at $z = w$ and w_{PB} is the hydrodynamic thickness of PB, which is determined from the condition of equality of the solvent flux,

$$J = \int_0^w \rho_s(z)\, v_s(z)\, dz = \int_{w_{PB}}^w \rho_s(z)\, v_m \left(1 - \frac{(w-z)^2}{(w-w_{PB})^2}\right) dz, \quad (4)$$

where $\rho_s(z)$ is the solvent density profile.

Introduction of the hydrodynamic thickness w_{PB} allows one to define the stationary (inside PB at $z < w_{PB}$) and mobile (outside PB at $z > w_{PB}$) phases within the channel and to use the mobile phase volume as the reference volume for the definition of the excess NP adsorption and, respectively, the Henry constant and the partition coefficient, as it is described below.

It is noteworthy that the PB conformation and its hydrodynamic thickness are determined by the solvent composition and do not depend on the magnitude of the force applied to the solvent[33] to simulate flow and on the channel width (see Supporting Information (SI), section I). This independence of the conditions of simulations implies the thermodynamic equilibrium between the solvent and PB and allows one to use the results of simulations for the channel of given width for predicting the partition coefficient and the retention time at other channel widths. The PB density $\rho_{PB}(z, w_{PB})$ can be considered as depending solely on the value of the hydrodynamic thickness, which is determined by the solvent composition, disregarding of the conditions of flow and the channel width. Respectively, provided the channel width w is reasonably larger than w_{PB} and the PBs of the opposite channel walls do not overlap, the solvent density can be calculated as $\rho_s(z) = \rho_0 - \rho_{PB}(z, w_{PB})$, as the solvent density in the bulk equals the overall bead density, $\rho_b = \rho_0$.

The hydrodynamic thickness w_{PB} of PB obtained from the parabolic approximation condition, Eq. (4), is the main parameter characterizing the PB conformation and the solvent flow at given solvent composition. Fig. 2c shows that w_{PB} is a non-linear function of the good

solvent fraction x_G with the expansion of the brush is becoming progressively pronounced as the good solvent fraction increases.

We have to compare the effects of the PB conformation at different solvent compositions on the NP adhesion and the separation at the condition of the constant flux of the solvent (J = const.) to mimic the conditions of chromatographic experiments. Note that regardless of the solvent composition and the respective PB conformation, the total amount of solvent in the channel cross-section is constant, $N_s = \int_o^w \rho_\mathrm{s}(z)dz \; = \int_0^w dz\,(\rho_\mathrm{b} - \rho_\mathrm{PB}\,(z)) = \rho_\mathrm{b} w - N_\mathrm{p} =$ const. Therefore, the condition of constant flux implies that the mean solvent velocity $\langle v_\mathrm{s}\rangle$ remains constant also,

$$\langle v_\mathrm{s}\rangle = \int_0^w \rho_\mathrm{s}(z)\, v_\mathrm{s}(z)\, dz \,/ \int_o^w \rho_\mathrm{s}(z)dz \;\; = \text{ const.} \tag{5}$$

The simulations at different solvent compositions are performed at the same force $g = 0.002\; k_\mathrm{B}T/R_\mathrm{c}$ applied on the solvent particles to create a steady flow. As a result, the simulated velocity magnitude and, respectively, the solvent flux increase as the solvent quality worsens, since the PB contracts, mobile zone outside PB widens, and the resistance to the flow decreases. In order to fulfill the condition of the constant mean solvent velocity and predict the flow at a given solvent flux from the simulation performed at a certain applied force, it is convenient to operate with the normalized velocity $v_\mathrm{n}(z)$ reduced by the mean flow velocity,

$$v_\mathrm{n}(z) = v_\mathrm{s}(z)/\langle v_\mathrm{s}\rangle \tag{6}$$

The use of the normalized velocity $v_\mathrm{n}(z)$ secures the equal flux condition Eq. (4) that is necessary for comparison of different separation regimes.

In the parabolic approximation, the normalized velocity $v_\mathrm{n}^\mathrm{PA}(z)$ is presented in the form,

$$v_{\mathrm{n}}^{\mathrm{PA}}(z) = \chi^{-1}\left(1 - \frac{(w-z)^2}{(w-w_{\mathrm{PB}})^2}\right) \quad (7)$$

Here, χ is the ratio of the mean flow velocity to the maximum velocity at given conditions, which depends on the PB hydrodynamic width w_{PB} and the channel width w as,

$$\chi(w_{\mathrm{PB}}, w) = \frac{2}{3N_{\mathrm{s}}}\rho_{\mathrm{bulk}}(w - w_{\mathrm{PB}}) - \frac{1}{N_{\mathrm{s}}}\int_{w_{\mathrm{PB}}}^{w}\rho_{\mathrm{PB}}(z, w_{PB})\left(1 - \frac{(w-z)^2}{(w-w_{\mathrm{PB}})^2}\right)dz, \quad (8)$$

see SI, section II for derivation. Eq. (7) is suitable for predicting the flow patterns in channels of arbitrary width w based on the PB density distribution characterized by the PB hydrodynamic thickness w_{PB} determined by the simulation of flow in the channel of a smaller width. The normalized velocity profiles are shown in Fig. 2b as solid lines in respective colors. In contrast to the velocities simulated at the same applied force, the magnitude of the normalized velocity decreases as the solvent quality worsens and PB contracts, because in order to keep the total flux (area under the curve) constant, the velocity needs to be decreased when the mobile zone within the channel widens.

III. II. Free energy landscapes of NP-PB adhesion. We determine the free energy landscape of NP adhesion to PB by performing free energy calculations using the ghost tweezers method,[45] (section II. IV) to analyze the specifics of NP adhesion to PB and to calculate the Henry constant of NP adsorption and partition coefficient between mobile and stationary phases. The free energy landscapes $A(z)$ of NP- PB interaction at different solvent quality $x_{\boldsymbol{G}}$, for NPs of different degree of hydrophilicity $x_{\boldsymbol{K}}$ with hydrophobic and hydrophilic ligands uniformly distributed over the NP surface are shown in Fig. 3a- b and in the SI, Fig.S4a-S4c. To calculate the free energy landscape, the force of NP-PB interaction F_{GT} obtained using the GT method is

integrated; the simulated force data is given in Figs. S2-S3 of the supporting information (SI, section III). The force data points are smoothened using a moving average prior to integration.

For all degrees of surface hydrophilicity x_K, the free energy landscapes show the same pattern and, with the decrease of solvent quality, exhibit a transition from repulsive, entropy-dominated, regime to adsorptive, enthalpy-dominated, regime with a deep well, of which minimum corresponds to the equilibrium adhesion state. At high x_G, the entropic repulsion dominates and is stronger for larger particles. At sufficiently low x_G, NPs are partially immersed into PB and enthalpic attraction prevails, being stronger for larger NPs, as the adhesion energy is generally proportional to the NP-PB interface area. This transition is associated with a reversal of the NP size dependence of the adhesion energy magnitude (the depth of the well at the equilibrium adhesion state) with respect to the NP size. In the case of purely hydrophobic NPs, this transition occurs around $x_G = 0.92$ (Fig. S4a, ref.33)

The transition between repulsion and attraction shifts towards a lower solvent composition with the NP hydrophilicity, as the overall repulsion between NPs and the PB increased further due to the increased presence of the hydrophilic ligands. The hydrophilic $\boldsymbol{K}$ ligands reduce adsorption of the hydrophobic polymer on NP surface and, at the same time, facilitate accommodation of poor solvent around NP, strengthening the NP-PB repulsion as x_K increases. In comparison with the free energy landscape of NP with solely hydrophobic ligands, (Fig. S4a), it can be inferred that NP adhesion is reduced as the fraction of hydrophilic ligands increases (Fig. 3a-b, Fig. S4b-c). Reduction of the solvent quality facilitates adsorption, but to a lower extent in comparison with NPs without hydrophilic ligands. At $x_K = 0.25$ (Fig. 3a), the

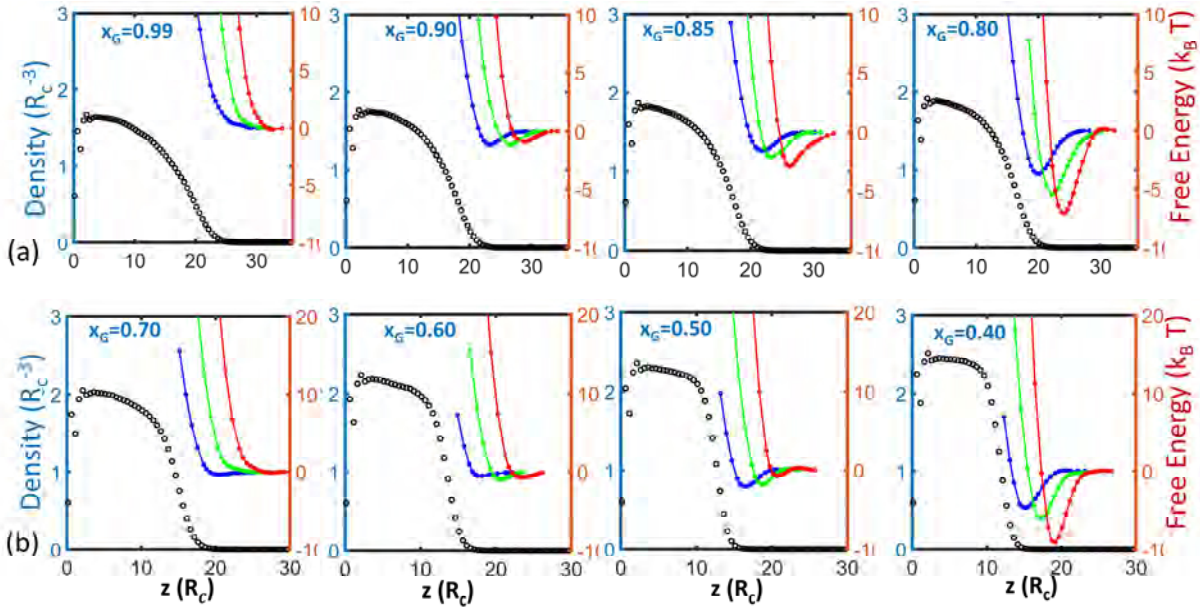

Figure 3. Free energy landscapes of NP-PB interaction at different good solvent fractions x_G in systems with degree of hydrophilicity (a) $x_K = 0.25$, (d) $x_K = 0.75$. The black curve indicates PB density $\rho_{PB}(z)$ and blue, green and red profiles give free energy $A(z)$ corresponding to $R_{NP} = 4\ R_c$, $6\ R_c$ and $8R_c$ respectively.

transition occurs around $x_G = 0.90$, and at $x_K = 0.5$ (Fig. S4b), it occurs around $x_G = 0.80$. The increase of hydrophilicity by grafting 50% ***K*** ligands on the NP surface causes the transition region to shift in the solvent quality x_G by about 10%. This shift becomes more pronounced for NPs with 75% of ***K*** ligands, as depicted in Fig. 3b. In this case, the strong adsorption mode occurs at as low as $x_G = 0.4$ and the transition around $x_G = 0.5$ lower by a 40% compared to the case of NPs with no ***K*** ligands.

With the most hydrophilic NPs, the adsorption regime occurs only at very low solvent qualities, at $x_G < 10\%$, see Fig. S4c. Even at $x_G = 0.2$, the repulsion dominates and strengthens with NP size. At $x_G = 0.01$, the lowest solvent quality considered, the strength of adsorption does not increase monotonically with NP size. At these low good solvent fractions, the poor solvent tends to wrap around the NP due to the solvation by ***K*** ligands and hinder the contact of polymers with NP surface. Additionally, the completely collapsed PBs become impenetrable as

the PB density becomes equal to the bulk density with a very sharp interfacial region with the bulk solvent. As a result, larger NPs cannot penetrate into PB and the number of PB-NP contacts and, respectively, the strength of adhesion does not increase with the NP size. For these reasons, a complete transition from repulsion to attraction regime with the reversal of order is not observed. Fig. 3 also shows that the repulsion to attractive transition is sharper for more hydrophobic particles: the range of x_G where the transition occurs widens with increase of x_K.

To demonstrate the effects of the PB density and chain length on NP adhesion, selected simulations are also performed with two other characteristic PB systems denoted as PB2 (grafting density of $0.36\ \mathrm{nm}^{-2}$ and chain length n_{seg} =160) and PB3 (same grafting density and $n_{\mathrm{seg}} = 200$). The respective force and free energy profiles of NP adhesion at $x_G = 0.01$ with $x_K = 1.0$ are given in SI, section III. The NP size dependence of the adsorption strength is found to be non-monotonic for PB2, as in the case of $x_K = 1.0$ for the system PB1, and monotonic for PB2 within the NP size range under consideration. Since PB2 has the lower grafting density compared to PB1 and the shorter chain length than PB3, PB2 should be more flexible and penetrable for NPs than PB1 and PB3.

III. III. Excess NP adsorption and Henry constant. The free energy landscape $A(z)$ determines the probability of NP to be at a specific distance z from the substrate that is proportional to the Boltzmann factor $\exp(-A(z)/k_{\mathrm{B}}T)$. Respectively, the NP density distribution is presented as,

$$\rho_{\mathrm{NP}}(z) = \rho_{\mathrm{NP}}^{\mathrm{b}} \exp(-A(z)/k_{\mathrm{B}}T), \qquad (9)$$

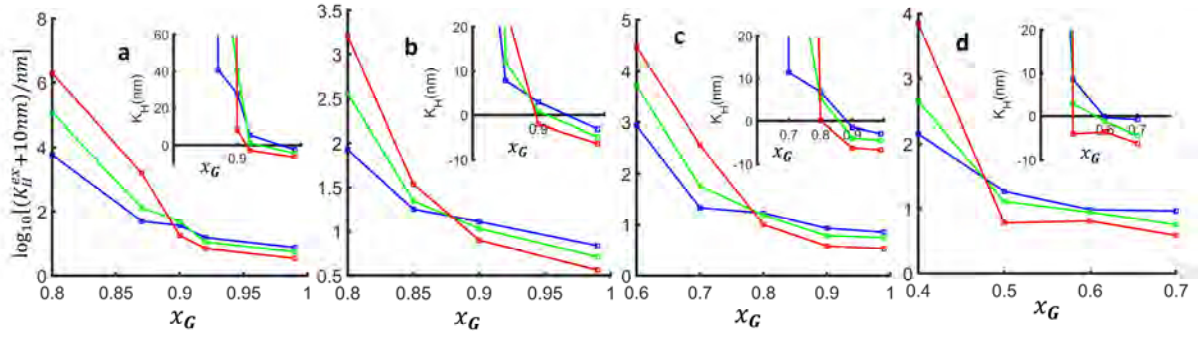

Figure 4. Logarithm of Henry constants of excess adsorption of NPs with different sizes and degree of hydrophilicity. (a) $x_K = 0$ (ref. 33) (b) $x_K = 0.25$ (c) $x_K = 0.5$ and (d) $x_K = 0.75$ at different solvent composition x_G. To avoid log of negative values of K_H^{ex} (in nm units) a constant of $10\ nm$ is added. Inset shows Henry constant values in the size exclusion mode and the transition region. The red curves indicate NPs of radius $8R_c$, while green and blue indicate $R_{NP} = 6\ R_c$ and $4R_c$ respectively.

where $\rho_{\mathrm{NP}}^{\mathrm{b}}$ is the NP density in the bulk solvent. As shown above, $A(z)$ depends on the PB conformation that is determined by the solvent composition and is independent of the solvent flow and the channel width provided that the latter sufficiently exceeds the PB width. Eq. (9) allows one to calculate the Henry constant and the partition coefficient between the mobile and stationary phases. The stationary phase boundary is defined by the PB hydrodynamic thickness, w_{PB}.

Division of the pore volume using the PB hydrodynamic thickness w_{PB} into stationary (inside PB at $z < w_{\mathrm{PB}}$) and mobile (outside PB at $z > w_{\mathrm{PB}}$) phases allows us to unambiguously introduce the NP excess adsorption, N_{ex}, as the difference between the total amount of NPs per unit substrate surface area, N_{tot}, and the amount of NPs in the reference volume of bulk solution equal to the volume of the mobile phase:[33]

$$N_{\mathrm{ex}} = N_{\mathrm{tot}} - \rho_{\mathrm{NP}}^{\mathrm{b}}(w - w_{\mathrm{PB}}) = \rho_{\mathrm{NP}}^{\mathrm{b}} \int_0^w e^{-\frac{A(z)}{k_{\mathrm{B}}T}} dz - \rho_{\mathrm{NP}}^{\mathrm{b}}(w - w_{\mathrm{PB}}) \qquad (10)$$

Accordingly, the Henry constant of excess adsorption is given by

$$K_{\mathrm{H}}^{\mathrm{ex}} = \frac{N_{\mathrm{ex}}}{\rho_{\mathrm{NP}}^{\mathrm{b}}} = \int_0^w e^{-\frac{A(z)}{k_{\mathrm{B}}T}} dz - (w - w_{\mathrm{PB}}) = w_{\mathrm{PB}} + \int_0^w \left(e^{-\frac{A(z)}{k_{\mathrm{B}}T}} - 1 \right) dz. \qquad (11)$$

The above definition of the NP excess adsorption implies that in the case of hydrodynamic chromatography (HDC) in the channels with hard walls in the absence of PB ($w_{\mathrm{PB}} = 0$), the excess adsorption is negative reflecting the exclusion of NPs from the near-surface layer of thickness equaled the NP radius R_{NP}. Respectively, the Henry constant, $K_{\mathrm{H}}^{\mathrm{ex}}$, is negative and equal to the NP radius, $K_{\mathrm{H}}^{\mathrm{ex}} = -R_{\mathrm{NP}}$, that reflects stronger repulsion of larger NPs.

The dependence of the excess adsorption Henry constant, $K_{\mathrm{H}}^{\mathrm{ex}}$, on the solvent quality for NPs of different size ($R_{\mathrm{NP}} = 4R_{\mathrm{c}}, 6R_{\mathrm{c}}$ and $8R_{\mathrm{c}}$) and degree of hydrophilicity $x_{\boldsymbol{K}} = 0$, 0.25, 0.5 and 0.75 is given in Fig. 4a-d. For convenience, logarithms of $K_{\mathrm{H}}^{\mathrm{ex}}$ with addition of a constant =10 nm are plotted, to avoid negative values at the repulsive good solvent conditions. While $K_{\mathrm{H}}^{\mathrm{ex}}$ is relatively small and negative ($\approx -R_{NP}$) when the NP-PB interaction is repulsive, it increases exponentially as the NP adsorption becomes stronger. At the solvent compositions where NP-adsorption is weak, $K_{\mathrm{H}}^{\mathrm{ex}}$ tend to decrease with NP size, while as the solvent quality worsens and NPs adsorb strongly to PB, the Henry constant increases with the NP size. For all systems considered, a transition is observed, as the solvent quality worsens, from the *size exclusion mode* of negative excess adsorption with larger particles repelled stronger to the *adsorption mode* with larger particles attracted stronger. As the NP hydrophilicity increases, this transition occurs at lower solvent quality, as discussed above (Fig. 3). As shown in the insets where $K_{\mathrm{H}}^{\mathrm{ex}}$ near the transition and the size exclusion regime are depicted, this transition takes place in a narrow range of $x_{\boldsymbol{G}}$, for NPs of given surface hydrophilicity regardless of their size, and one can identify the characteristic "critical" condition reminiscent to the critical point of adsorption (CPA) in polymer chromatography. The dependence of such critical transition solvent quality on the NP hydrophilicity is discussed below.

III. IV. Absolute adsorption and partition coefficient. While the excess adsorption allows for a rigorous thermodynamic consideration of NP adhesion, in order to analyze the NP separation in the solvent flow, one needs to identify the amount of retained or immobile NPs, or, in other words to define the absolute adsorption. Following the conventional assumption of the hydrodynamics chromatography and assuming that NPs, which are located within distance $z < w_{\mathrm{PB}} + R_{\mathrm{NP}}$ from the substrate and partially immersed into PB, are immobile, the absolute adsorption is defined as

$$N_{\mathrm{abs}} = \rho_{\mathrm{NP}}^{\mathrm{b}} \int_0^{w_{\mathrm{PB}}+R_{\mathrm{NP}}} e^{-\frac{A(z)}{k_{\mathrm{B}}T}} dz \tag{12}$$

Respectively, the Henry constant of absolute adsorption is defined as the ratio of the number NPs retained in the PB stationary phase (at $z < w_{\mathrm{PB}} + R_{\mathrm{NP}}$) per substrate unit area to the NP bulk concentration,

$$\begin{aligned} K_{\mathrm{H}} &= \int_0^{w_{\mathrm{PB}}+R_{\mathrm{NP}}} \exp(-A(z)/k_{\mathrm{B}}T)\, dz \\ &= \int_0^{w_{PB}+R_{NP}} [\exp(-A(z)/k_{\mathrm{B}}T) - 1] dz + w_{\mathrm{PB}} + R_{\mathrm{NP}} \end{aligned} \tag{13}$$

The Henry constant of absolute adsorption K_{H} differs from the Henry constant of excess adsorption $K_{\mathrm{H}}^{\mathrm{ex}}$ and is always non-negative. In the size exclusion mode, $K_{\mathrm{H}} \approx K_{\mathrm{H}}^{\mathrm{ex}} + R_{\mathrm{NP}}$. This approximate equality holds when the PB has a sharp boundary at w_{PB}, so that $A(z)$ is negligibly small beyond $w_{\mathrm{PB}} + R_{\mathrm{NP}}$. Note that in the case of hydrodynamic chromatography in hard wall channels without PB coating, $A(z) = \infty$ at $z < R_{\mathrm{NP}}$ and the absolute adsorption Henry constant vanishes, $K_{\mathrm{H}} = 0$, in contrast to the excess adsorption Henry constant being negative, $K_{\mathrm{H}}^{\mathrm{ex}} =$

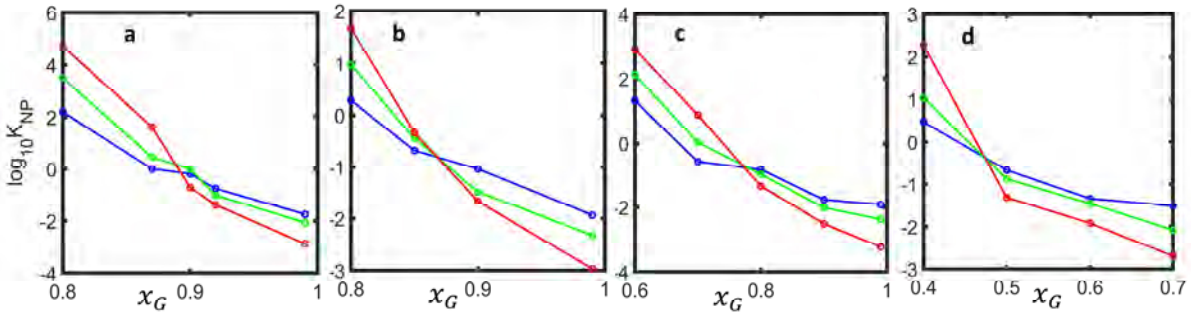

Figure 5. The partition coefficient K_{NP} of the nanoparticles as a function of the good solvent fraction x_G at different fraction of K ligands on NP surfaces. (a) $x_K = 0.0$, (b) $x_K = 0.25$, (c) $x_K = 0.5$ and (d) $x_K = 0.75$. Colors: red, green and blue data correspond to NP sizes $R_{NP} = 8R_c$, $6R_c$ and $4R_c$ respectively. The channel half width w is 70.43 R_c.

$-R_{\mathrm{NP}}$. The difference between absolute and excess NP adsorption is discussed in detail in Supporting Information, Section IV.

Although the Henry constant (Eq. 13) is determined in the free energy simulations performed in the channel of a particular width, this thermodynamic quantity does not depend on the system size provided that it is larger than the simulated system.

The partition coefficient in liquid chromatography is generally defined as the ratio of the solute concentration in the immobile stationary phase to the solute concentration in the mobile bulk phase, However, in the system considered here with the PB stationary phase and highly inhomogeneous NP distribution at the PB-solvent interphase, it is more practical to define the apparent partition coefficient K_{NP} as the ratio of the total amount of NPs retained in the PB stationary phase at $z < w_{\mathrm{PB}} + R_{\mathrm{NP}}$ and the amount of NP in the bulk mobile phase of width $(w - w_{\mathrm{PB}} - R_{\mathrm{NP}})$,

$$K_{\mathrm{NP}} = K_{\mathrm{H}}/(w - w_{\mathrm{PB}} - R_{\mathrm{NP}}) \tag{14}$$

(see SI, section IV). In contrast to the Henry constant K_{H} that has the dimension of length, the partition coefficient K_{NP} is dimensionless. K_{NP} characterizes the fraction of retained NPs in the pore of given width w.

The partition coefficient defined by Eq. (14) is calculated as a function of the good solvent fraction for NPs of different sizes and surface hydrophilicities characterized by $x_{\boldsymbol{K}}$. The results are shown in Fig. 5a-d, which present the logarithm of K_{NP} as a function of the solvent quality $x_{\boldsymbol{G}}$ for NPs of different hydrophilicity ($x_{\boldsymbol{K}} = 0.0, 0.25, 0.5$ and 0.75) and size ($R_{\mathrm{NP}} = 4\,R_{\mathrm{c}},\ 6\,R_{\mathrm{c}}$ and $8R_{\mathrm{c}}$) in the channel of $w = 70.43\,R_{\mathrm{c}} = 50$ nm. In all cases, the partition coefficient monotonically decreases with the increase of the solvent quality from adsorption mode to size exclusion mode. The transition from one mode to the other occurs at different solvent composition for NPs with different surface hydrophilicity. This should be expected given the $A(z)$ and $K_{\mathrm{H}}^{\mathrm{ex}}$ depicted in Figs. 3-4. However, the partition coefficient depends on the channel width w, while the Henry constant is independent of it. The CPAs obtained from values of K_{NP} corresponding to the transition shown in Fig. 5 are discussed below.

It is worth noting, that for NPs functionalized solely by hydrophilic ligands, $x_{\boldsymbol{K}} = 1$, the NP-PB the partition coefficient K_{NP} may be non-monotonic with respect to the NP size at certain PB density and chain length. As shown in SI, section III, such non-monotonic dependence is related to the fact that adsorption of hydrophilic NPs may take place only at very low solvent qualities (Fig. 3e) due to PB-ligand repulsion and solvation of $\boldsymbol{K}$-ligands by the poor solvent. This shows that critical conditions may not be observed in all systems.

III. V. Critical conditions of size-independent NP elution. The introduction of the PB hydrodynamic thickness w_{PB} that identifies the boundary between the stationary and mobile

phases makes it possible to model NP adhesion and flow in wider channels based on the simulation data obtained in a channel of a particular width. To this end, we employ the approximate model of NP transport accepted in the hydrodynamic chromatography.[52-54] The velocity of NPs located in the mobile phase beyond the exclusion volume boundary $w_{\mathrm{PB}} + R_{\mathrm{NP}}$ is assumed equal to the solvent velocity, while the velocity of NPs located inside this boundary is zero. Within the parabolic approximation (Eq. (7)), the normalized (with respect to the mean solvent velocity) velocity of the NP located at the distance z from the substrate, $v_{\mathrm{p}}(z)$, is presented as

$$v_{\mathrm{p}}(z) = v_{\mathrm{n}}^{\mathrm{PA}}(z), \text{for } w_{\mathrm{PB}} + R_{\mathrm{NP}} < z \leq w \text{ and } 0 \ \ for \ 0 \leq \ z \leq w_{\mathrm{PB}} + R_{\mathrm{NP}} \qquad (15)$$

The hydrodynamic approximation implies that NP is effectively adsorbed and immobile if it is immersed into PB even partially with its center located at $z < w_{\mathrm{PB}} + R_{\mathrm{NP}}$ that is in line with the definition of the absolute adsorption and the Henry constant given by Eq. (13).

For a comparative analysis, the solvent retention time $t_{\mathrm{s}} = L/\langle v_{\mathrm{n}} \rangle$ that is kept constant, where L is the length of the chromatographic column, is taken as the reference and the NP retention time t_{p} is presented in dimensionless units,

$$\tau_{\mathrm{p}} = t_{\mathrm{p}} \, / t_{\mathrm{s}} = 1/\langle v_{\mathrm{p}} \rangle \qquad (16)$$

Here, $\langle v_{\mathrm{p}} \rangle$ is the mean normalized velocity of NPs that is given by the convolution of the NP normalized velocity $v_{\mathrm{p}}(z)$ and the probability of the NP location at distance z from the substrate,

$$\langle v_p \rangle = \frac{\int_{w_{\mathrm{PB}}+R_{\mathrm{NP}}}^{w} \exp(-A(z)/k_{\mathrm{B}}T) \ v_{\mathrm{p}}(z) \, dz}{\int_{0}^{w} \exp(-A(z)/k_{\mathrm{B}}T) \, dz} \qquad (17)$$

Eq. (17) can be simplified further assuming that $A(z) \approx 0$ in the whole region of mobile phase at $z > w_{\mathrm{PB}} + R_{\mathrm{NP}}$, and respectively, the concentration of NP in the mobile phase can be substituted by the bulk concentration. In this case,

$$\langle v_p \rangle \approx \frac{\int_{w_{\mathrm{PB}}+R_{\mathrm{NP}}}^{w} v_{\mathrm{p}}(z)\, dz}{K_{\mathrm{H}} + (w - w_{\mathrm{PB}} - R_{\mathrm{NP}})} = \frac{v_\lambda}{1 + K_{\mathrm{NP}}} \tag{18}$$

Here, v_λ is the normalized mean velocity in the limiting hydrodynamic regime of purely repulsive (i. e, with $K_{\mathrm{H}} = 0$) NPs, that is related to the ratio $\lambda = R_{\mathrm{NP}}/(w - w_{\mathrm{PB}})$ of the NP radius R_{NP} to the half width of the mobile phase, as

$$v_\lambda = \chi^{-1} \frac{2}{3}\left(1 + \lambda - \frac{\lambda^2}{2}\right) \tag{19}$$

where the factor χ is defined by Eq. (8). Detailed derivation of the above equation is given in SI, section V.

Eqs. (16-19) provide the sought relationship between the retention time and the NP size and partition coefficient for given solvent composition:

$$\tau_{\mathrm{p}} = 1/\langle v_{\mathrm{p}} \rangle = (1 + K_{\mathrm{NP}})\tau_\lambda \tag{20}$$

where $\tau_\lambda = 1/v_\lambda$ is the minimum retention time of purely repulsive NPs in the hydrodynamic regime. This relationship combines the size exclusion effects characterized by τ_λ and the NP- PB interaction effects characterized by the partition coefficient K_{NP}.

Fig. 6a presents the mean NP velocity in a slit-like channel, normalized with respect to the volumetric solvent flow, assuming parabolic approximation within a channel of width 100 nm ($w = 70.43\ R_c$), as a function of the solvent quality for NPs of different size ($R_{\mathrm{NP}} = 4\ R_{\mathrm{c}}, 6R_{\mathrm{c}}$ and $8R_{\mathrm{c}}$) and degree of hydrophilicity, $x_{\boldsymbol{K}}$ of 0.0, 0.25, 0.5 and 0.75. $\langle v_{\mathrm{p}} \rangle$ values are calculated using Eq. (18) for a range of $x_{\boldsymbol{G}}$ with a resolution of 0.001, by interpolating and extrapolating the K_H values between and beyond the simulated data points. For $x_{\boldsymbol{K}} = 0$, the K_H values are further smoothed. In all cases, the NP velocity $\langle v_{\mathrm{P}} \rangle$ decreases as $x_{\boldsymbol{G}}$ decreases starting from the hydrodynamic limit, first, rather slowly at high solvent quality and then more sharply near the CPA transition point. In all the four cases, $\langle v_{\mathrm{P}} \rangle$ reverses the order of its dependence on

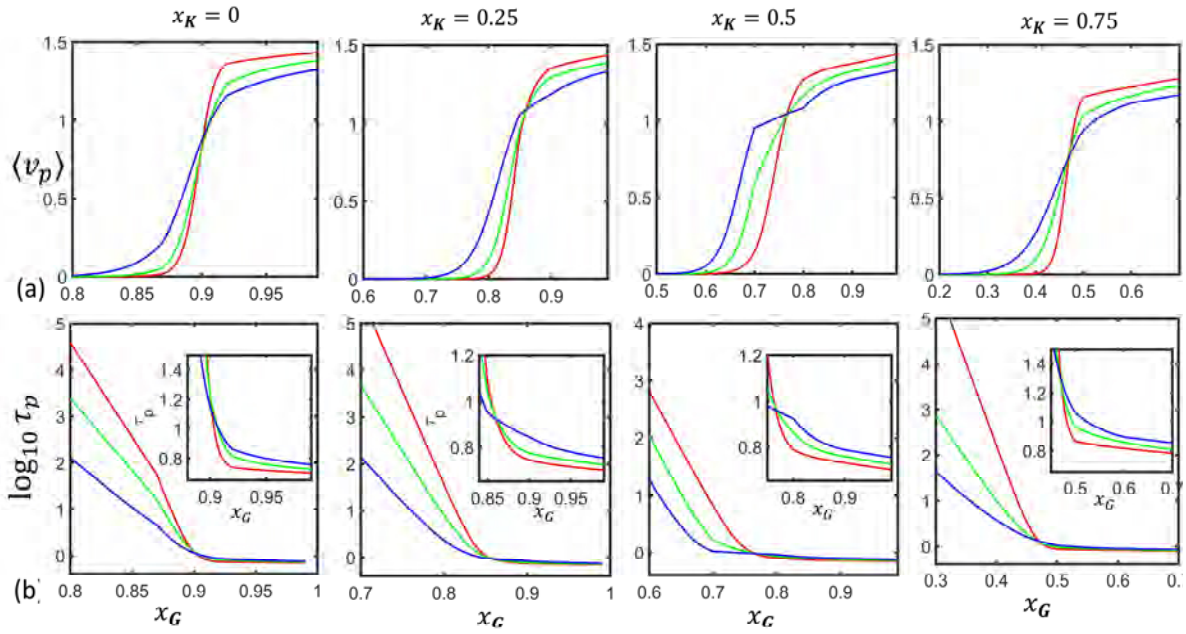

Figure 6. (a) Variation of mean nanoparticle velocity $\langle v_p \rangle$ with solvent quality in systems containing NPs with different K ligand densities x_K. (b) The ratio of NP retention time to the solvent retention time (τ_p) corresponding to (a). Inserts show variation of τ_p near the transition point and the size exclusion regime. Colors indicate NP size, R_{NP}; red-8R_c, green - 6R_c and blue - 4R_c.

NP size as x_G decreases, while going from a size-exclusion mode, where $\langle v_P \rangle$ increases with NP size, to the adsorption mode, where $\langle v_P \rangle$ decreases with NP size and eventually diminishes to zero due to strong adsorption. Note that the transition becomes sharper as NP size increases. This reversal occurs in compliance with the reversal of the thermodynamic partition coefficient at the CPA transition conditions.

Note that in the size exclusion mode, the mean NP velocity is always larger than the mean solvent velocity (that is used as the reference unit for normalization) due to two factors accounted in Eq. (18). Firstly, similarly to the hydrodynamic chromatography, NPs are excluded from the low velocity region of width R_{NP} at the PB boundary. Secondly, solvent partially penetrates into the PB stationary phase and its average velocity is smaller the mobile phase velocity as characterized by the factor χ, Eq. (8). In Fig. 6a, with $w = 70.43\ R_c$, the NP velocity in the size-exclusion mode is ~1.45 for the largest NP, while in the simulations with $w =$

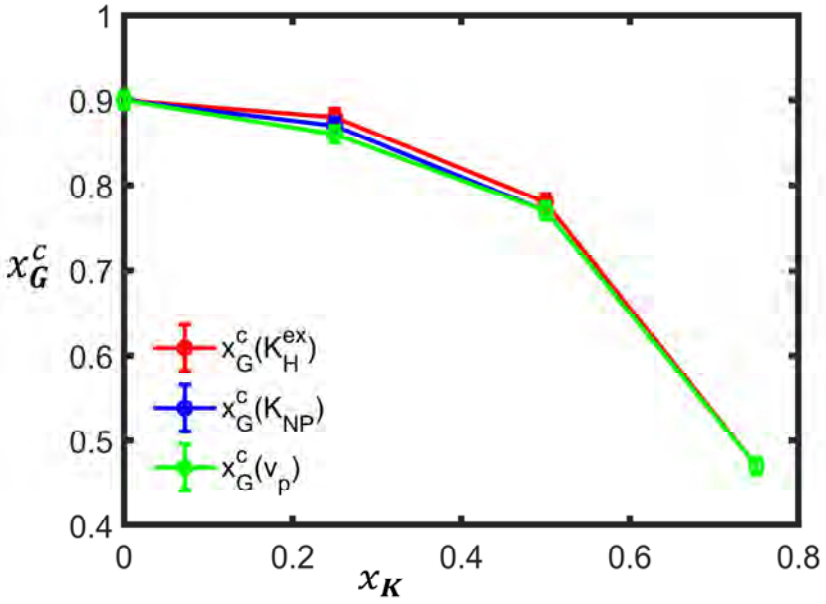

Figure 7. The NP critical point of adsorption calculated by three definitions: From the equality of thermodynamic Henry constant of excess adsorption K_H^{ex}(red), from the NP partition coefficient (K_{NP}) in a channel of half width 50 nm (blue) and the equality of mean NP velocities (green).

33.38 R_c, the NP velocity is ~2.8 (see SI, section V). Consequently, the NP retention time is shorter than the solvent retention time.

Fig. 6b presents the relative retention time τ_p as a function of the solvent quality x_G for NPs of different hydrophilicity, $x_K = 0.0, 0.25, 0.5$ and 0,75. The relative retention time decreases with the increase of solvent quality and undergoes a transition from adsorption to size-exclusion mode with the reversal of the sequence of elution. While in the adsorption mode (poor solvent quality) $\tau_p \gg 1$ due to adsorption effects, in the size-exclusion mode (good solvent quality), $\tau_p < 1$, since the NP mean velocity exceeds that of the solvent. The inserts zoom-in the region around $\tau_p \sim 1$ where the CPA transition, at which the elution time is independent of the NP size, takes place.

The above analysis presents critical conditions of NP adsorption and separation, in three ways: (1) the thermodynamic definition of the CPA based on the reversal of the NP size

dependence of the Henry constant $K_{\mathrm{H}}^{\mathrm{ex}}$ of excess adsorption (Fig. 4), (2) the chromatographic (based on the pore volume partition on mobile and stationary phases) definition using the size-independence of the partition coefficient K_{NP} (Fig. 5), and (3) the hydrodynamic definition using the mean NP velocity $\langle v_{\mathrm{p}} \rangle$ or the retention time τ_{p} (Fig. 6). While the thermodynamic definition of CPA depends on the PB characteristics and NP surface chemistry and is independent of the channel width, the other two CPAs depend on the width of the channel by virtue of Eqs. (14) and (18). However, it turns out that the dependence of CPA on channel width is negligible for range of channel widths of interest for which $\lambda \ll 1$. Fig. 7 shows the differently estimated dependencies of the CPA solvent composition $x_{\boldsymbol{G}}^{\mathrm{c}}$ as on the NP hydrophilicity $x_{\boldsymbol{K}}$. The CPA values defined by different methods are practically similar within the accuracy of our simulations. CPAs obtained from the equality of $K_{\mathrm{H}}^{\mathrm{ex}}$ (red points) are slightly different from that of other two methods for $x_{\boldsymbol{K}} = 0.25$ and 0.5, however, the deviations are small and can be attributed to the fact that, unlike in other two cases, $K_{\mathrm{H}}^{\mathrm{ex}}$ is calculated not requiring that $A(z) = 0$ for $z > w_{PB} + R_{NP}$. From the reversal regions of the partition coefficient. $x_{\boldsymbol{G}}^{\mathrm{c}} = 0.90 \pm 0.01$ for the case of $x_{\boldsymbol{K}} = 0$, while with $x_{\boldsymbol{K}} = 0.25$, the transition appears to occur at a solvent composition 0.87 ± 0.01. For higher hydrophilicities, $x_{\boldsymbol{G}}^{\mathrm{c}} = 0.77 \pm 0.01$ at 50% hydrophilic ligand fraction x, about 13% lower than the completely hydrophobic particles and $x_{\boldsymbol{G}}^{\mathrm{c}} = 0.47 \pm 0.015$, for 75% ***K***-ligands, which is 48% smaller. These values remain practically the same as the CPAs obtained by the equality of the mean NP velocities. Regardless of the method, the estimated CPA strongly and non-linearly depends on the NP surface chemistry. Although the CPA values were estimated just for four distinct fractions of hydrophilic ligands, the interpolated $x_{\boldsymbol{G}}^{c}$ - $x_{\boldsymbol{K}}$ dependence can be used for predicting the critical adsorption conditions for NP of intermediate hydrophilicity.

III. VI. Macroscopic model of elution time distribution in the isocratic regime. Our simulations suggest that PB conformation characterized by the hydrodynamic width and NP adhesion characterized by the Henry constant are determined by the solvent composition and are independent of the solvent flow rate and the pore size. Further assumption that the solvent flow can be approximated by the parabolic velocity profile beyond the PB hydrodynamic width makes possible to predict NP elution in the channels of arbitrary size based on the simulations performed in a particular pore geometry with dimensions smaller than those of practical chromatographic supports.

Let's consider the elution time distributions in PB-grafted channels of cylindrical shape, that is a conventional model representation of the pore space geometry in separation media in hydrodynamic chromatography. When the channel radius w is sufficiently large, the surface curvature effects can be neglected and the PB conformation and NP adhesion can be characterized by the same hydrodynamic width w_{PB} and Henry constant as simulated in the slit-like channel of a smaller width. Accordingly, we further assume that in a PB-grafted cylindrical channel the solvent flow in the mobile phase (at $r \leq w - w_{PB}$) is approximated by the Poiseuille profile in the cylindrical tube of radius $w - w_{PB}$

$$v_{\mathrm{s}}(r) = 2\bar{v}\,(1 - r^2/(w - w_{\mathrm{PB}})^2), \tag{21}$$

where $\bar{v}$ is the mean velocity of the solvent in the mobile phase, r is the radial coordinate. Like in the case of the slit-like channel, we define the mean solvent velocity across the channel,

$$\langle v_s \rangle = \frac{\int_0^{w-w_{PB}} \rho_{\mathrm{s}}(r) v_{\mathrm{s}}(r) r\, dr}{\int_0^{w} \rho_{\mathrm{s}}(r) r\, dr} = 2\,\bar{v}\,\chi_r \tag{22}$$

Eq. (22) implies the cylindrical symmetry of the distributions of solvent and PB densities, ($\rho_{\mathrm{s}} = \rho_{\mathrm{s}}(r);\ \rho_{\mathrm{PB}} = \rho_{\mathrm{PB}}(r)$). The dimensionless factor χ_r is given by

$$\chi_r = \frac{\int_0^{w-w_{PB}} \rho_{\mathrm{s}}(r)\left(1 - \frac{r^2}{(w - w_{\mathrm{PB}})^2}\right) r\, dr}{\int_0^{w} \rho_s(r) r\, dr} \tag{23}$$

The normalized velocity of the solvent equals $v_{\mathrm{n}}(r) = v_{\mathrm{s}}(r)/\langle v_{\mathrm{s}}\rangle = \chi_r^{-1}(1 - r^2/(w - w_{\mathrm{PB}})^2)$, which means that the mean normalized solvent velocity $\langle v_{\mathrm{n}}\rangle = 1$. As such, χ_r^{-1} represents the maximum normalized solvent velocity.

To estimate the distribution of elution time due to axial dispersion of NP along the column due to the non-uniform (Poiseuille-like) solvent flow we employ the First Passage Time (FPT) distribution model[55-57] that implies an equilibrium distribution of NPs between the mobile and stationary phases characterized by the apparent partition coefficient K_{NP} (Eq. (14)), which in for cylindrical channel takes the following form,

$$K_{\mathrm{NP}} = K_{\mathrm{H}}\, S/V_m = 2K_{\mathrm{H}}/(w - w_{\mathrm{PB}} - R_{\mathrm{NP}}). \tag{24}$$

Here, $S = 2\pi(w - w_{\mathrm{PB}} - R_{\mathrm{NP}})L$ and $V_m = \pi\,(w - w_{\mathrm{PB}} - R_{\mathrm{NP}})^2\, L$ are the surface area and the volume of the core of the channel of radius $z = w - w_{\mathrm{PB}} - R_{\mathrm{NP}}$ and length L, available for unretained NPs. The FPT model presents the elution time distribution in the form of the inverse Gaussian distribution, which in the dimensionless variables of time reduced to the solvent retention time t_{s} and the axial length reduced to column length L, takes the form[56-57]

$$g(\tau) = \frac{1}{\sqrt{4\pi\ \bar{E}_{\mathrm{NP}}\tau^3}} \exp\left(-\frac{\left(1 - \tau/\tau_{\mathrm{p}}\right)^2}{4\ \bar{E}_{\mathrm{NP}}\tau}\right) \tag{25}$$

where $\bar{E}_{\mathrm{NP}}$ is the reduced longitudinal (axial) dispersion coefficient, $\bar{E}_{\mathrm{NP}} = E_{\mathrm{NP}}t_{\mathrm{s}}/L^2$. The detailed derivation of Eq. (25) is given in supporting information section VI.

In the purely hydrodynamic limit ($A(z) = 0$), the mean NP velocity in the channel is found to be (see SI, section VII)

$$\langle v_{\mathrm{p}} \rangle = \frac{\chi_r^{-1}}{2}(1 + 2\lambda - \lambda^2) = \bar{v}_0\, v_\lambda, \tag{26}$$

where $\bar{v}_0 = \chi_r^{-1}/2$ is the mean velocity of solvent in the mobile phase. Note that $\bar{v}_0$ is different from mean solvent velocity $\langle v_{\mathrm{n}} \rangle = 1$, due to the stagnant solvent inside the PB immobile phase. It should be noted that Eq. (26) was suggested for NP flow in channel with solid walls, and the existence of the PB may invoke additional effects such as NP rotation that cause them to move with a velocity lower than the local solvent velocity.[53, 58] These effects however should be analyzed, and the existing approximate approaches are limited to solid particles in hard wall channels. In the case when NP adsorption is present, following the existing methodology,[59] it can be shown that (see SI, section VII)

$$\langle v_{\mathrm{p}} \rangle = \bar{v}_0\, v_\lambda/(1 + K_{\mathrm{NP}}) \tag{27}$$

Thus,

$$\tau_{\mathrm{p}} = 1/\langle v_{\mathrm{p}} \rangle = (1 + K_{\mathrm{NP}})/\bar{v}_0\, v_\lambda = (1 + K_{\mathrm{NP}})\tau_\lambda, \tag{28}$$

where τ_λ is the NP retention time in the hydrodynamic (no adsorption) limit in a cylindrical channel of radius $w - w_{\mathrm{PB}}$. The major contribution to the NP dispersion comes from the convective diffusion characterized by the Taylor-Aris[60-61] axial dispersion coefficient E_{NP}. The E_{NP} dependence on the NP size and the partition coefficient can be incorporated following the works of Brenner and coworkers[53,59, 62] (see SI, section VII)

$$E_{\mathrm{NP}} = \frac{\bar{v}_0^2}{48 D_{\mathrm{NP}}}(w - w_{\mathrm{PB}})^2\,(1 - 1.862\,\lambda + 9.68\,\lambda^2)\,\frac{1 + 6K_{\mathrm{NP}} + 11K_{\mathrm{NP}}^2}{(1 + K_{\mathrm{NP}})^3} \tag{29}$$

Here, D_{NP} is the NP diffusion coefficient related to the NP radius through the Stokes-Einstein equation. In Eq. (29), the polynomial dependence on λ was obtained by Brenner and

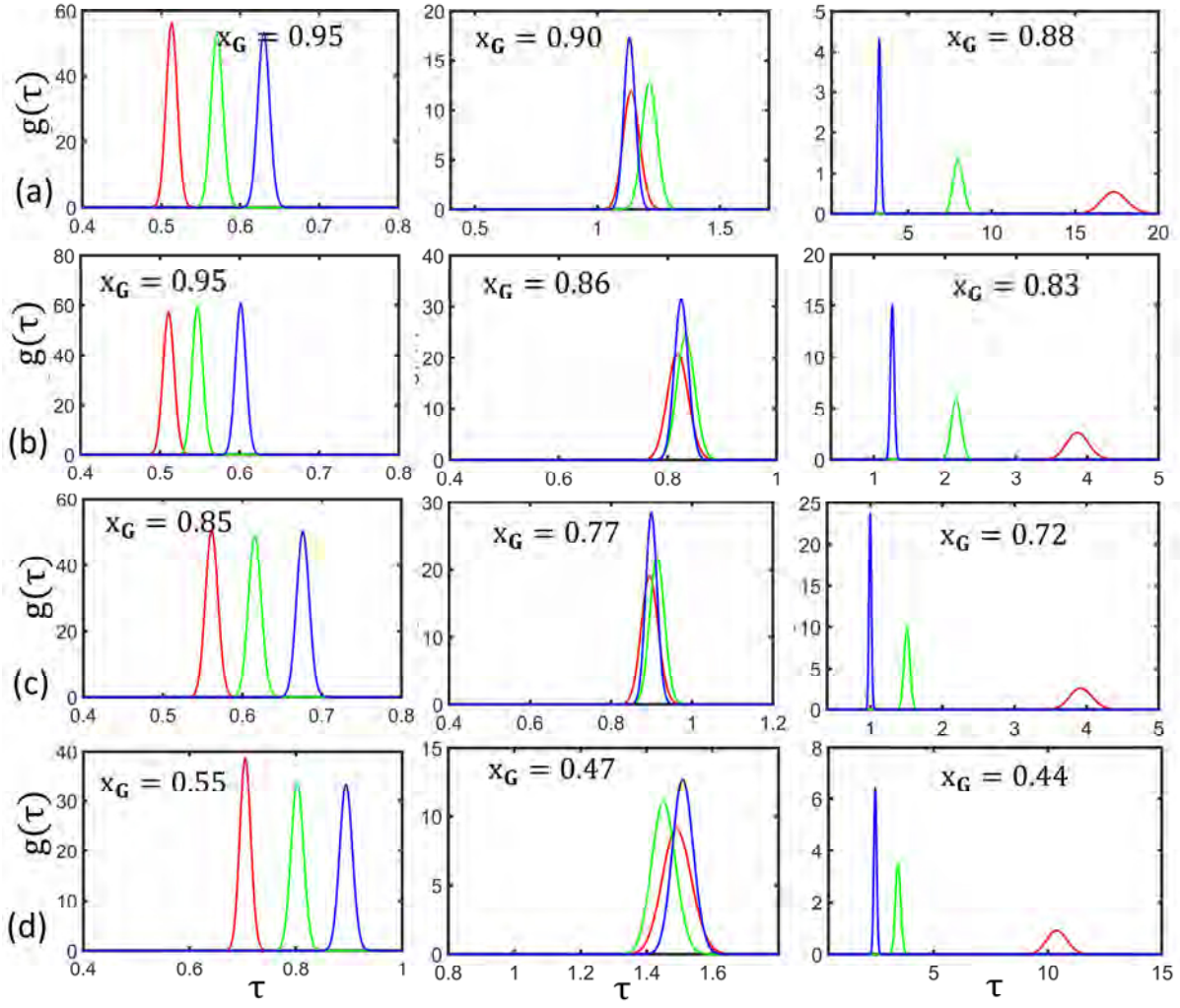

Figure 8. Elution time distribution $g(\tau)$ of NPs calculated via the first passage convective diffusion model, Eqs. (25, 29), in a column of length $L = 3.34$ cm with cylindrical channels of radius $w = 50$ nm. Calculations are performed for NPs of size $R_{NP} = 5.68$ nm (red), 4.26 nm (green) and 2.84 nm (blue) and hydrophilicity x_K equal to (a) 0.0, (b) 0.25, (c) 0.5 and (d) 0.75 at different solvent composition x_G. Transition from the size-exclusion (central column) and adsorption (right column) regimes with the reversal of the sequence of elution occurs as x_G decreases and the solvent quality worsens. The central column shows the CPA conditions of size-independent elution.

Gaydos[53] from considerations of hydrodynamic effects on the particle motion and diffusion in a cylindrical pore with smooth hard walls and spherical NPs. A detailed derivation of Eq. (29) is given in SI, section VII.

Fig. 8 presents the calculated isocratic elution time distributions for NP separation in the PB-grafted cylindrical channel of radius $w = 70.43\ R_c = 50$ nm at different solvent conditions.

The values of the partition coefficient K_{NP}, the maximum normalized solvent velocity χ_r^{-1} and the PB hydrodynamic thickness w_{PB} are obtained as functions of the solvent quality x_G by the appropriate interpolation and extrapolation of the data given in Fig. 6. The value of the column length $L = 4.7 \times 10^7\ R_c$ (3.34 cm) is taken to get the distinct distributions, (see SI, section VII, for more detail) Fig. 8a-d shows elution distributions for NP of different hydrophobicity, $x_K = 0.0, 0.25$, 0.5 and 0.75. The positions of the peaks correspond to the mean retention times for each particular size and type. The size exclusion mode that is observed at relatively high solvent quality exhibit distinct retention times, which decrease with the NP size. The reduction of solvent quality leads to the CPA conditions where the elution time distributions for NPs of different size overlap with insignificant deviation of the retention times. When the solvent quality is reduced further, the retention times increase dramatically in the adsorption mode, with the reversed order of elusion. Noteworthy, the CPA conditions of size independent NP elution found at the distinct values of solvent composition (0.90, 0.86, 0.77 and 0.47) depending on the NP surface chemistry ($x_K = 0.25, 0.5$ and 0.75, respectively), which within the accuracy of our simulations correspond to the same estimates shown in Fig.7.

III. VII. NP separation in the gradient mode of elution. In interaction polymer chromatography,[26] the gradient elution with temporal variation of the solvent composition is found more efficient in separating polymers according to their chemical composition than the isocratic elution.[30] In the linear gradient mode, $x_G = x_G^0 + at$, where x_G^0 is the initial solvent composition at $t = 0$ and $a = dx_G/dt$ is the solvent composition gradient that is kept constant. The gradient mode of elution is based on the strong dependence of the elution time t_{p} on the solvent composition x_G in the isocratic mode, $t_{\mathrm{p}} = t_{\mathrm{p}}(x_G)$. Let us assume that the solute

components of different chemistry can be ranged with respect to the solvent compositions, $x_{\mathbf{G}}^{c}$, corresponding to their CPA conditions in the isocratic mode. This means that the retention time t_{p} for a particular component sharply reduces in the vicinity of the respective CPA solvent composition $x_{\boldsymbol{G}} = x_{\boldsymbol{G}}^{\mathrm{c}}$ from long retention times in the adsorption regime at $x_{\boldsymbol{G}} < x_{\boldsymbol{G}}^{\mathrm{c}}$ to much shorter times in the size exclusion regime at $x_{\boldsymbol{G}} > x_{\boldsymbol{G}}^{0}$. In the gradient elution mode, one starts with a mobile phase composition $x_{\boldsymbol{G}}^{0}$ in which all solute components are adsorbed strongly to the stationary phase so that the retention times are longer than the time of experiment. This implies that the initial composition is beyond the range of the CPA solvent compositions of all the components, $x_{\boldsymbol{G}}^{0} < x_{\boldsymbol{G}}^{\mathrm{c}}$. Then, the solvent composition is varied keeping the solvent volumetric flow constant; $x_{\boldsymbol{G}}$ gradually increases and the solute fractions desorb from the stationary phase and elute with respect to their CPA solvent compositions. The solute fraction of given chemistry desorbs and start moving once $x_{\boldsymbol{G}}$ approaches the respective value of $x_{\boldsymbol{G}}^{c}$ with a small difference in "take off" times, $t_{\uparrow}$ around $(x_{\boldsymbol{G}}^{0} - x_{\boldsymbol{G}}^{\mathrm{c}})/a$, for the fraction components of different size, which eventually elute within a relatively narrow range of retention times. As a result, the fractions of different chemistry are separated with a minimal deviation of the retention times which necessarily arises due to the difference in size and effects of longitudinal dispersion.

The theory of the gradient elution[63-68] relates the mean retention time t_{p}^{g} of a particular component in the gradient mode to the isocratic retention time $t_{\mathrm{p}}(x_{\boldsymbol{G}})$ that is a known function of the solvent composition $x_{\boldsymbol{G}}$. Assuming that the solvent composition is varied in time according to a certain function $x_{\boldsymbol{G}}(t)$, with the solvent retention time t_{s} kept constant, the mean retention time t_{p}^{g} in the gradient mode is calculated from the following integral equation,[68]

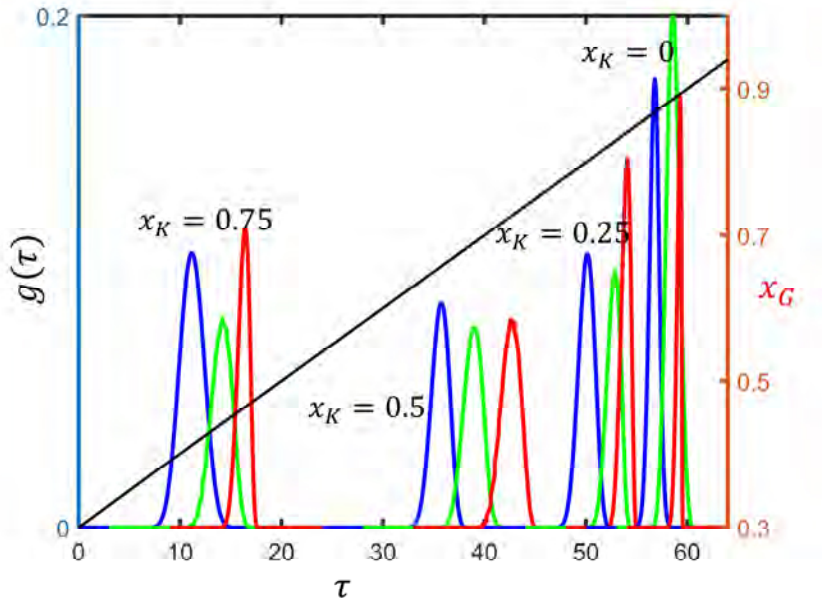

Figure 9.The NP elution time distributions in the gradient mode. Starting from the initial solvent composition at $x_g^0 = 0.3$, NPs of different surface chemistry x_K is eluted at different times. The solvent composition is varied with time at a constant rate shown as the black line. Red, green and blue respectively represent particle sizes R_{NP} equal to $8R_c$. $6R_c$ and $4R_c$ respectively.

$$\int_0^{t_{\mathrm{p}}^{\mathrm{g}}-t_{\mathrm{s}}} \frac{dt}{t_{\mathrm{p}}(x_{\boldsymbol{G}}(t)) - t_{\mathrm{s}}} = 1 \tag{30}$$

A detailed derivation of Eq. (30) is given in SI, Section VIII.

Extending the FPT model, the retention time distribution in the gradient mode can be estimated by the shifted inverse Gaussian distribution

$$g(\tau) = \frac{1}{\sqrt{4\pi\, \bar{E}_{\mathrm{NP}}(\tau - \tau_{\uparrow})^3}} \exp\left(-\frac{\left(1 - (\tau - \tau_{\uparrow})/(\tau_{\mathrm{p}}^{g} - \tau_{\uparrow})\right)^2}{4\ \bar{E}_{\mathrm{NP}}(\tau - \tau_{\uparrow})} \right) \tag{31}$$

Eq. (31) is written using dimensionless time $\tau = t/t_{\mathrm{s}}$ and all temporal parameters are reduced respective to the solvent retention time t_{s}. Here, $\tau_{\uparrow} = t_{\uparrow}/t_{\mathrm{s}}$ is the reduced "take-off" time and $\bar{E}_{\mathrm{NP}}$ is the reduced dispersion coefficient for given component. Note that the "take-off" time $t_{\boldsymbol{G}}^{\uparrow}$ is defined from the expert assumption that $x_{\boldsymbol{G}}^{\uparrow} = x_{\boldsymbol{G}}(t_{\boldsymbol{G}}^{\uparrow})$ corresponds to the solvent

composition at which given component desorbs from the stationary phase. The dispersion coefficient is calculated according to Eq. (29) at the solvent composition close to $x_{\boldsymbol{G}}^{\mathrm{c}}$, $E_{\mathrm{NP}} = E_{\mathrm{NP}}(x_{\boldsymbol{G}}^{\mathrm{c}})$.

Fig. 9 depicts the inverse Gaussian distributions given by Eq. (31) during the gradient elution of NPs with different sizes and surface chemistry $x_{\boldsymbol{K}}$ in a cylindrical channel of radius $w = 70.43\ R_{\mathrm{c}}$. To obtain these profiles, we set $dx_{\boldsymbol{G}} = 0.0002$ and $dt = 0.02$ (rate of composition change $\frac{dx_{\boldsymbol{G}}}{dt} = 0.01$) while the elution starts with a solvent composition $x_{\boldsymbol{G}}^{0} = 0.3$. The black line shows the change in solvent composition in the course of elution. The NPs of sizes $R_{\mathrm{NP}} = 4\ R_{\mathrm{c}}$, $6\ R_c$ and $8R_{\mathrm{c}}$ and surface chemistry $x_{\boldsymbol{K}} = 0.75, 0.5, 0.25$ and 0 are in the mobile phase in equal proportions. The take-off composition for each NPs in each case of $x_{\boldsymbol{K}}$ is taken according to the velocity curves, at a point where the NP starts moving, different for different NPs. The distributions are calculated for NP velocities smaller than the solvent velocity (see SI, section VIII).

As shown in the Fig. 9, the NPs elute with retention times that depends on their degree of hydrophilicity in the reverse order. The retentions times are well-separated according to their degree of hydrophobicity, and the NPs of different sizes having the same hydrophilicity elute within a small range of solvent composition. These results clearly indicate that the surface chemistry-specific NP separation can be efficiently achieved on PB-grafted substrates employing the gradient mode of elution. It is worth noting that the separation efficiency is affected by the broadness of the NP size distribution. Here, we model relatively small NPs of several nm in diameter within a relatively narrow size range. The quality of separation would worsen if the size distribution were broader. NPs considered in this work are functionalized by hydrophobic and hydrophilic ligands with relatively weak interaction potentials that do not include any specific

intermolecular interactions with polymer and solvent (e.g. dissociation with formation of charged groups).

IV. Conclusions

We considered separation of NPs functionalized by different types of ligands in PB-grafted channels, by varying the binary solvent composition and confirmed our hypothesis about the existence of critical point of adsorption (CPA) in such system. The CPA is defined as the particular solvent composition, which corresponds to the transition between the size exclusion and adsorption modes and depends on the NP surface chemistry. Note that in contrast to polymer adsorption, the introduced CPA of NP adhesion to PB is not related to any critical phenomenon, rather it indicates a condition of the observed sharp transition from the entropy-dominated to the enthalpy-dominated regimes leading to the reversal of the size-dependent order of elution. Extensive DPD simulations are performed to investigate the effects of the NP surface chemistry on NP adhesion and flow in PB-grafted pore channels in binary solvents of different composition. We considered NPs functionalized by two different types of ligands, which are modeled as short hydrophobic and hydrophilic chains grafted on the NP surface. By varying the ligand composition, we mimic different surface chemistries and control the NP-PB adhesion interaction. We analyze the specifics of solvent flow through PB-grafted channels and quantify the conformation and sorption capacity of the PB stationary phase depending on the solvent composition by introducing the hydrodynamic PB thickness as the stationary phase boundary. The NP-PB adhesion is quantified in terms of the free energy landscape calculated using the ghost tweezers (GT) method, which determines the Henry constant of NP adsorption, the partition coefficient, and ultimately the NP retention time, depending on the solvent and ligand

compositions. The distributions of NP retention time are analyzed using the convective diffusion model, in the isocratic and gradient elution modes. The relationship is established between the CPA solvent composition and the NP ligand composition that points toward a possibility of NP separation by surface chemistry in the gradient mode of elution by varying the solvent composition as it is done in the interaction polymer chromatography.

Supporting information.

Supporting information to this manuscript includes the following. Simulations of the PB density and solvent flow in slit channels of different width are described in Section I. Dependence of the ratio between the mean and maximum solvent velocity of the solvent velocity profiles on solvent and polymer brush density, channel width and PB effective height. Eq. 8 is derived in Section II. Dependence of the effective force between the NP and PB on NP location for different systems is presented in section III. The excess adsorption of NPs and its relevance to the partition coefficient is described in Section IV. Section V contains the derivation the mean velocity of NP in a slit-like channel (Eq. 19 of the paper) and gives the mean velocity in different systems. Section VI describes the elution time distributions in terms of the first passage time. Section VII describes NP transport in cylindrical channels in terms of mean velocity and the mean axial dispersion coefficient. Finally, Section VIII relates the NP mobilities in the channel to the predicted retention time distributions in the gradient elution NP chromatography. Supporting materials are available free of charge at XXX.

Acknowledgements

This work was funded by the National Science Foundation CBET grant “GOALI: Theoretical Foundations of Interaction Nanoparticle Chromatography”, No 510993, and used computational

resources of Extreme Science and Engineering Discovery Environment (XSEDE) supported by the National Science Foundation grant No ACI-1548562.

References

1. Anker, J. N.; Hall, W. P.; Lyandres, O.; Shah, N. C.; Zhao, J.; Van Duyne, R. P., Biosensing with Plasmonic Nanosensors. *Nat. Mater.* **2008,** *7* (6), 442-453.
2. Klajn, R.; Browne, K. P.; Soh, S.; Grzybowski, B. A., Nanoparticles That "Remember" Temperature. *Small* **2010,** *6* (13), 1385-1387.
3. Tanaka, K.; Chujo, Y., Design of Functionalized Nanoparticles for the Applications in Nanobiotechnology. *Adv. Powder Technol.* **2014,** *25* (1), 101-113.
4. Nakanishi, H.; Grzybowski, B. A., Supercapacitors Based on Metal Electrodes Prepared from Nanoparticle Mixtures at Room Temperature. *J. Phys. Chem. Lett.* **2010,** *1* (9), 1428-1431.
5. Bliznyuk, V.; Ruhstaller, B.; Brock, P. J.; Scherf, U.; Carter, S. A., Self-Assembled Nanocomposite Polymer Light-Emitting Diodes with Improved Efficiency and Luminance. *Adv. Mater.* **1999,** *11* (15), 1257-1261.
6. Park, J. H.; Lim, Y. T.; Park, O. O.; Kim, J. K.; Yu, J.-W.; Kim, Y. C., Polymer/Gold Nanoparticle Nanocomposite Light-Emitting Diodes: Enhancement of Electroluminescence Stability and Quantum Efficiency of Blue-Light-Emitting Polymers. *Chem. Mater.* **2004,** *16* (4), 688-692.
7. Hasobe, T.; Imahori, H.; Kamat, P. V.; Ahn, T. K.; Kim, S. K.; Kim, D.; Fujimoto, A.; Hirakawa, T.; Fukuzumi, S., Photovoltaic Cells Using Composite Nanoclusters of Porphyrins and Fullerenes with Gold Nanoparticles. *J. Am. Chem. Soc.* **2005,** *127* (4), 1216-1228.
8. Sun, B.; Marx, E.; Greenham, N. C., Photovoltaic Devices Using Blends of Branched CdSe Nanoparticles and Conjugated Polymers. *Nano Lett.* **2003,** *3* (7), 961-963.
9. Tseng, R. J.; Tsai, C.; Ma, L.; Ouyang, J.; Ozkan, C. S.; Yang, Y., Digital Memory Device Based on Tobacco Mosaic Virus Conjugated with Nanoparticles. *Nat. Nanotechnol.* **2006,** *1* (1), 72-77.
10. Peer, D.; Karp, J. M.; Hong, S.; Farokhzad, O. C.; Margalit, R.; Langer, R., Nanocarriers as an Emerging Platform for Cancer Therapy. *Nat. Nanotechnol.* **2007,** *2* (12), 751-760.
11. Roy, I.; Ohulchanskyy, T. Y.; Pudavar, H. E.; Bergey, E. J.; Oseroff, A. R.; Morgan, J.; Dougherty, T. J.; Prasad, P. N., Ceramic-Based Nanoparticles Entrapping Water-Insoluble Photosensitizing Anticancer Drugs: A Novel Drug−Carrier System for Photodynamic Therapy. *J. Am. Chem. Soc.* **2003,** *125* (26), 7860-7865.
12. Williams, S.; Neumann, A.; Bremer, I.; Su, Y.; Dräger, G.; Kasper, C.; Behrens, P., Nanoporous Silica Nanoparticles as Biomaterials: Evaluation of Different Strategies for the Functionalization with Polysialic Acid by Step-by-step Cytocompatibility Testing. *J. Mater. Sci. - Mater. Med.* **2015,** *26*, 125.
13. Kowalczyk, B.; Lagzi, I.; Grzybowski, B. A., Nanoseparations: Strategies for Size and/or Shape-selective Purification of Nanoparticles. *Curr. Opin. Colloid Interface Sci.* **2011,** *16* (2), 135-148.

14. Itoh, N.; Sano, A.; Santa, T.; Kato, M., Simultaneous Analysis of Nanoparticles and Small Molecules by High-performance Liquid Chromatography Using a Silica Monolithic Column. *Analyst* **2014,** *139* (18), 4453-4457.
15. Robertson, J. D.; Rizzello, L.; Avila-Olias, M.; Gaitzsch, J.; Contini, C.; Magoń, M. S.; Renshaw, S. A.; Battaglia, G., Purification of Nanoparticles by Size and Shape. *Sci. Rep.* **2016,** *6*, 27494.
16. Ute, K.; Yoshida, S.; Kitayama, T.; Bamba, T.; Harada, K.; Fukusaki, E.; Kobayashi, A.; Ishizuka, N.; Minakuchi, H.; Nakanishi, K., Size Exclusion Chromatography of Standard Polystyrenes with a Wide Range of Molecular Weight Up to 7.45[times]106 on Monolithic Silica Capillary Columns. *Polym. J* **2006,** *38* (11), 1194-1197.
17. Wei, G.-T.; Liu, F.-K., Separation of Nanometer Gold Particles by Size Exclusion Chromatography. *J. Chromatogr. A* **1999,** *836* (2), 253-260.
18. Striegel, A. M.; Brewer, A. K., Hydrodynamic Chromatography. *Annu. Rev. Anal. Chem.* **2012,** *5* (1), 15-34.
19. Malysheva, A.; Lombi, E.; Voelcker, N. H., Bridging the Divide Between Human and Environmental Nanotoxicology. *Nat. Nanotechnol.* **2015,** *10* (10), 835-844.
20. Lee, J.-S.; Stoeva, S. I.; Mirkin, C. A., DNA-Induced Size-Selective Separation of Mixtures of Gold Nanoparticles. *J. Am. Chem. Soc.* **2006,** *128* (27), 8899-8903.
21. Albanese, A.; Tang, P. S.; Chan, W. C. W., The Effect of Nanoparticle Size, Shape, and Surface Chemistry on Biological Systems. *Annu. Rev. Biomed. Eng.* **2012,** *14* (1), 1-16.
22. Kim, S. T.; Saha, K.; Kim, C.; Rotello, V. M., The Role of Surface Functionality in Determining Nanoparticle Cytotoxicity. *Acc. Chem. Res.* **2013,** *46* (3), 681-691.
23. Paget, V.; Dekali, S.; Kortulewski, T.; Grall, R.; Gamez, C.; Blazy, K.; Aguerre-Chariol, O.; Chevillard, S.; Braun, A.; Rat, P.; Lacroix, G., Specific Uptake and Genotoxicity Induced by Polystyrene Nanobeads with Distinct Surface Chemistry on Human Lung Epithelial Cells and Macrophages. *PLOS ONE* **2015,** *10* (4), e0123297.
24. Pasch, H.; Trathnigg, B., In *Multidimensional HPLC of Polymers*, Springer Berlin Heidelberg: Berlin, Heidelberg, 2013; pp 27-35.
25. Brun, Y.; Foster, P., Characterization of Synthetic Copolymers by Interaction Polymer Chromatography: Separation by Microstructure. *J. Sep. Sci.* **2010,** *33* (22), 3501-3510.
26. Brun, Y.; Rasmussen, C. J., Chapter 11 - Interaction polymer chromatography. In *Liquid Chromatography (Second Edition)*, Fanali, S.; Haddad, P. R.; Poole, C. F.; Riekkola, M.-L., Eds. Elsevier: 2017; pp 275-318.
27. Guttman, C. M.; Di Marzio, E. A.; Douglas, J. F., Influence of Polymer Architecture and Polymer−Surface Interaction on the Elution Chromatography of Macromolecules through a Microporous Media. *Macromolecules* **1996,** *29* (17), 5723-5733.
28. Brun, Y., The Mechanism of Copolymer Retention in Interactive Polymer Chromatography. I. Critical Point of Adsorption for Statistical Copolymers. *J. Liq. Chromatogr. Related Technol.* **1999,** *22* (20), 3027-3065.
29. Brun, Y., The Mechanism of Copolymer Retention in Interactive Polymer Chromatography. Ii. Gradient Separation. *J. Liq. Chromatogr. Related Technol.* **1999,** *22* (20), 3067-3090.
30. Brun, Y.; Alden, P., Gradient Separation of Polymers at Critical Point of Adsorption. *J. Chromatogr. A* **2002,** *966* (1–2), 25-40.

31. Cimino, R. T.; Rasmussen, C. J.; Brun, Y.; Neimark, A. V., Critical Conditions of Polymer Adsorption and Chromatography on Non-porous Substrates. *J. Colloid Interface Sci.* **2016,** *474*, 25-33.
32. Cimino, R. T.; Rasmussen, C. J.; Brun, Y.; Neimark, A. V., Mechanisms of Chain Adsorption on Porous Substrates and Critical Conditions of Polymer Chromatography. *J. Colloid Interface Sci.* **2016,** *481*, 181-193.
33. Santo, K. P.; Vishnyakov, A.; Brun, Y.; Neimark, A. V., Adhesion and Separation of Nanoparticles on Polymer-Grafted Porous Substrates. *Langmuir* **2018,** *34* (4), 1481-1496.
34. Ayres, N., Polymer Brushes: Applications in Biomaterials and Nanotechnology. *Polym. Chem.* **2010,** *1* (6), 769-777.
35. Kumar, S. K.; Benicewicz, B. C.; Vaia, R. A.; Winey, K. I., 50th Anniversary Perspective: Are Polymer Nanocomposites Practical for Applications? *Macromolecules* **2017,** *50* (3), 714-731.
36. Crosby, A. J.; Lee, J. Y., Polymer Nanocomposites: The "Nano" Effect on Mechanical Properties. *Polym. Rev.* **2007,** *47* (2), 217-229.
37. Paul, D. R.; Robeson, L. M., Polymer Nanotechnology: Nanocomposites. *Polymer* **2008,** *49* (15), 3187-3204.
38. Kreer, T., Polymer-brush Lubrication: A Review of Recent Theoretical Advances. *Soft Matter* **2016,** *12* (15), 3479-3501.
39. Witten, T. A.; Pincus, P. A., Colloid Stabilization by Long Grafted Polymers. *Macromolecules* **1986,** *19* (10), 2509-2513.
40. Borukhov, I.; Leibler, L., Enthalpic Stabilization of Brush-Coated Particles in a Polymer Melt. *Macromolecules* **2002,** *35* (13), 5171-5182.
41. Striolo, A.; Egorov, S. A., Steric Stabilization of Spherical Colloidal Particles: Implicit and Explicit Solvent. *J. Chem. Phys.* **2007,** *126* (1), 014902.
42. Prokhorova, S. A.; Kopyshev, A.; Ramakrishnan, A.; Zhang, H.; Rühe, J., Can Polymer Brushes Induce Motion of Nano-objects? *Nanotechnology* **2003,** *14* (10), 1098.
43. Arita, T.; Yoshimura, T.; Adschiri, T., Size Exclusion Chromatography of Quantum Dots by Utilizing Nanoparticle Repelling Surface of Concentrated Polymer Brush. *Nanoscale* **2010,** *2* (8), 1467-1473.
44. Cheng, J.; Vishnyakov, A.; Neimark, A. V., Morphological Transformations in Polymer Brushes in Binary Mixtures: DPD Study. *Langmuir* **2014,** *30* (43), 12932-12940.
45. Cheng, J.; Vishnyakov, A.; Neimark, A. V., Adhesion of Nanoparticles to Polymer Brushes Studied with the Ghost Tweezers Method. *J. Chem. Phys.* **2015,** *142* (3), 034705.
46. Groot, R. D.; Warren, P. B., Dissipative Particle Dynamics: Bridging the Gap Between Atomistic and Mesoscopic Simulation. *J. Chem. Phys.* **1997,** *107* (11), 4423-4435.
47. Hoogerbrugge, P. J.; Koelman, J. M. V. A., Simulating Microscopic Hydrodynamic Phenomena with Dissipative Particle Dynamics. *Europhys. Lett.* **1992,** *19* (3), 155.
48. Español, P.; Warren, P., Statistical Mechanics of Dissipative Particle Dynamics. *Europhys. Lett.* **1995,** *30* (4), 191.
49. Graupner, K.; Winter, E. R. S., 201. Some Measurements of the Self-diffusion Coefficients of Liquids. *J. Chem. Soc.* **1952,** (0), 1145-1150.
50. Plimpton, S., Fast Parallel Algorithms for Short-Range Molecular Dynamics. *J. Comput. Phys.* **1995,** *117* (1), 1-19.
51. Humphrey, W.; Dalke, A.; Schulten, K., VMD: Visual Molecular Dynamics. *J. Mol. Graphics* **1996,** *14* (1), 33-38.

52. DiMarzio, E. A.; Guttman, C. M., Separation by Flow. *Macromolecules* **1970,** *3* (2), 131-146.
53. Brenner, H.; Gaydos, L. J., The Constrained Brownian Movement of Spherical Particles in Cylindrical Pores of Comparable Radius. *J. Colloid Interface Sci.* **1977,** *58* (2), 312-356.
54. Prieve, D. C.; Hoysan, P. M., Role of Colloidal Forces in Hydrodynamic Chromatography. *J. Colloid Interface Sci.* **1978,** *64* (2), 201-213.
55. Yang, S.; Neimark, A. V., Critical Conditions of Polymer Chromatography: An Insight from SCFT Modeling. *J. Chem. Phys.* **2013,** *138* (24), 244903.
56. Oxtoby, J. C., Stochastic Models for Chromatography. *J. Chem. Phys.* **1969,** *51* (9), 3886-3890.
57. Felinger, A., Molecular Dynamic Theories in Chromatography. *J. Chromatogr. A* **2008,** *1184* (1), 20-41.
58. Brenner, H., Pressure Drop Due to the Motion of Neutrally Buoyant Particles in Duct Flows. *J. Fluid Mech.* **1970,** *43* (4), 641-660.
59. Dill, L. H.; Brenner, H., A General Theory of Taylor Dispersion Phenomena: III. Surface Transport. *J. Colloid Interface Sci.* **1982,** *85* (1), 101-117.
60. Aris, R., On the Dispersion of a Solute in a Fluid Flowing Through a Tube. *Proc. R. Soc. London, Ser. A* **1956,** *235* (1200), 67-77.
61. Taylor, G., Dispersion of Soluble Matter in Solvent Flowing Slowly Through a Tube. *Proc. R. Soc. London, Ser. A* **1953,** *219* (1137), 186-203.
62. Brenner, H., Macrotransport Processes. *Langmuir* **1990,** *6* (12), 1715-1724.
63. Freiling, E. C., Ion Exchange as a Separations Method. IX. Gradient Elution Theory. *J. Am. Chem. Soc.* **1955,** *77* (8), 2067-2071.
64. Freiling, E. C., Gradient Elution Theory. *J. Phys. Chem.* **1957,** *61* (5), 543-548.
65. Snyder, L. R., Linear Elution Adsorption Chromatography: VII. Gradient Elution Theory. *J. Chromatogr. A* **1964,** *13*, 415-434.
66. Jandera, P.; Churacek, J., *Gradient Elution in Liquid Chromatography. Theory and Practice*. Elsevier: Amsterdam, 1985.
67. Drake, B., Theory of Gradient Elution Analysis *Arkiv. Kemi* **1955,** *8*, 1-21.
68. Nikitas, P.; Pappa-Louisi, A., Expressions of the Fundamental Equation of Gradient Elution and a Numerical Solution of These Equations under Any Gradient Profile. *Anal. Chem.* **2005,** *77* (17), 5670-5677.

TOC graphic

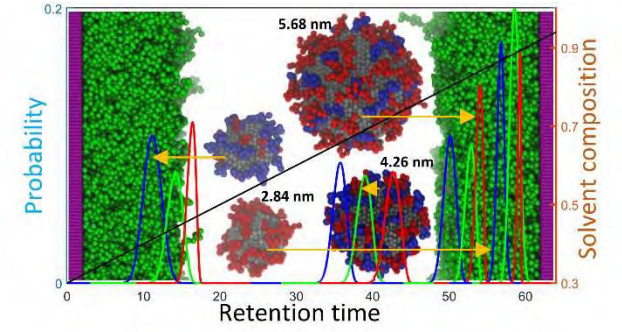
5.68 nm
4.26 nm
2.84 nm
Probability
Solvent composition
Retention time
0.2
0
0.9
0.7
0.5
0.3
0
10
20
30
40
50
60